

Evaluation and development of deep neural networks for image super-resolution in optical microscopy

Chang Qiao^{1,5}, Di Li^{2,5}, Yuting Guo^{2,5}, Chong Liu^{2,3,5}, Tao Jiang^{2,3}, Qionghai Dai¹✉ and Dong Li^{2,3,4}✉

Deep neural networks have enabled astonishing transformations from low-resolution (LR) to super-resolved images. However, whether, and under what imaging conditions, such deep-learning models outperform super-resolution (SR) microscopy is poorly explored. Here, using multimodality structured illumination microscopy (SIM), we first provide an extensive dataset of LR-SR image pairs and evaluate the deep-learning SR models in terms of structural complexity, signal-to-noise ratio and upscaling factor. Second, we devise the deep Fourier channel attention network (DFCAN), which leverages the frequency content difference across distinct features to learn precise hierarchical representations of high-frequency information about diverse biological structures. Third, we show that DFCAN's Fourier domain focalization enables robust reconstruction of SIM images under low signal-to-noise ratio conditions. We demonstrate that DFCAN achieves comparable image quality to SIM over a tenfold longer duration in multicolor live-cell imaging experiments, which reveal the detailed structures of mitochondrial cristae and nucleoids and the interaction dynamics of organelles and cytoskeleton.

Deep learning has brought about significant breakthroughs in a variety of image transformation tasks. In particular, it has greatly advanced single-image super-resolution (SISR), which aims to restore a high-resolution (HR) photorealistic image from its LR counterpart^{1–9}. Deep-learning SISR models have been applied recently to enhance the resolution of scientific microscopy images^{10–12}, indicating their great potential to revolutionize the future development of SR microscopy. Compared with SISR applications in enhancing the textures of macroscale realistic photographs, super-resolving microscopy images for scientific analysis demands greater accuracy and quantifiability of the inferred nanoscale structures. However, it remains uncertain to what extent the information conveyed by deep-learning-based super-resolution (DLSR) images can be utilized for quantitative analysis and under what conditions DLSR approaches outperform conventional SR microscopy. Here, we employed our home-built multimodality structured illumination microscopy (SIM) system, which integrates total internal reflection fluorescence (TIRF-SIM), grazing incidence (GI-SIM)¹³ and nonlinear SIM¹⁴ (Methods) to acquire well-matched LR-SR image pairs across wide ranges of signal-to-noise ratio (SNR) levels of input LR images, complexity of the observed biological structures and desired upscaling factors. This dataset is named BioSR and has been made publicly available.

The training of DLSR networks can be viewed as a process of extracting the high-dimensional features that bridge the LR and SR image spaces⁶. It is known that the power spectrum of an input LR image is restricted below the diffraction-limited frequency (Supplementary Note 1), so we speculate that leveraging the frequency content difference across distinct features in the Fourier domain, rather than structural differences in the spatial domain,

might enable the DLSR networks to learn the hierarchical representations of high-frequency information more precisely and efficiently. Inspired by the spatial domain channel attention mechanism employed in the deep residual channel attention network (RCAN)^{5,15}, we developed DFCAN and its derivative trained with generative adversarial network (GAN) strategy, termed DFGAN. We show that the both DFCAN and DFGAN are able to infer SR images of diverse biological structures more precisely than state-of-the-art DLSR networks. Moreover, we exploit the capability of DFCAN and DFGAN to model the interdependencies between informative feature maps in the Fourier domain for robust SIM reconstruction, even under imaging conditions of relatively low SNR and high background fluorescence. We demonstrate that DFCAN-SIM and DFGAN-SIM can reconstruct high-quality SR live-cell images, capturing the minute yet highly dynamic interactions between intracellular organelles and cytoskeleton over an extended timecourse relative to conventional SIM.

Results

Experimental dataset acquisition for DLSR method training and evaluation. We employed a multimodal SIM system to acquire a dataset of clathrin-coated pits (CCPs), endoplasmic reticulum (ER), microtubules (MTs) and F-actin filaments, which represent increasing structural complexity (Supplementary Fig. 1). For each type of specimen, we acquired about 50 sets of raw SIM images at ten escalating levels of excitation light intensity. In particular, at the highest excitation level, we ensured that the SNR of all raw images was high enough to reconstruct superior quality SIM images^{13,16} (Extended Data Fig. 1 and Supplementary Fig. 2). Each set of raw SIM images was averaged out to a diffraction-limited wide-field (WF) image

¹Department of Automation, Tsinghua University, Beijing, China. ²National Laboratory of Biomacromolecules, CAS Center for Excellence in Biomacromolecules, Institute of Biophysics, Chinese Academy of Sciences, Beijing, China. ³College of Life Sciences, University of Chinese Academy of Sciences, Beijing, China. ⁴Bioland Laboratory, Guangzhou Regenerative Medicine and Health Guangdong Laboratory, Guangzhou, China. ⁵These authors contributed equally: Chang Qiao, Di Li, Yuting Guo, Chong Liu. ✉e-mail: qhda@tsinghua.edu.cn; lidong@ibp.ac.cn

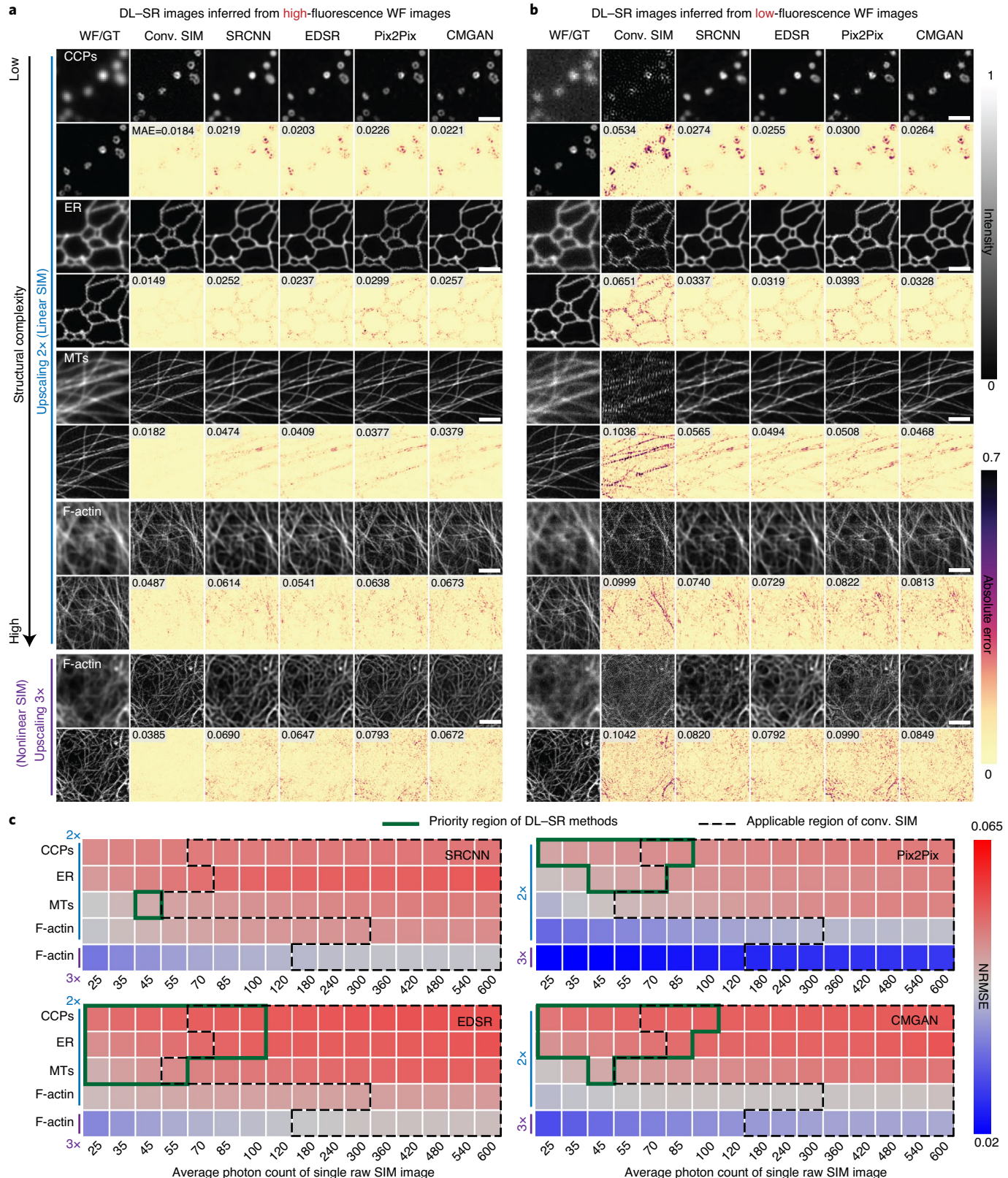


Fig. 1 | Evaluation of the four DLSR models. **a,b**, Representative SISR images inferred from single WF diffraction-limited images of high (**a**) and low (**b**) fluorescence. Conventional SIM (Conv. SIM) images of the same ROI are shown for reference. The difference images relative to GT are below the corresponding DLSR images. The mean absolute error (MAE) is labeled at the top left of each difference image. Scale bar, 0.75 μ m for CCPs; 1 μ m for other specimens. **c**, Assessment matrices of the four DLSR models in terms of NRMSE illustrating their priority regions (green) and the applicable region of Conv. SIM (dashed black). Gamma value, 0.6 for the F-actin images of upscaling 3 \times in **a** and **b**.

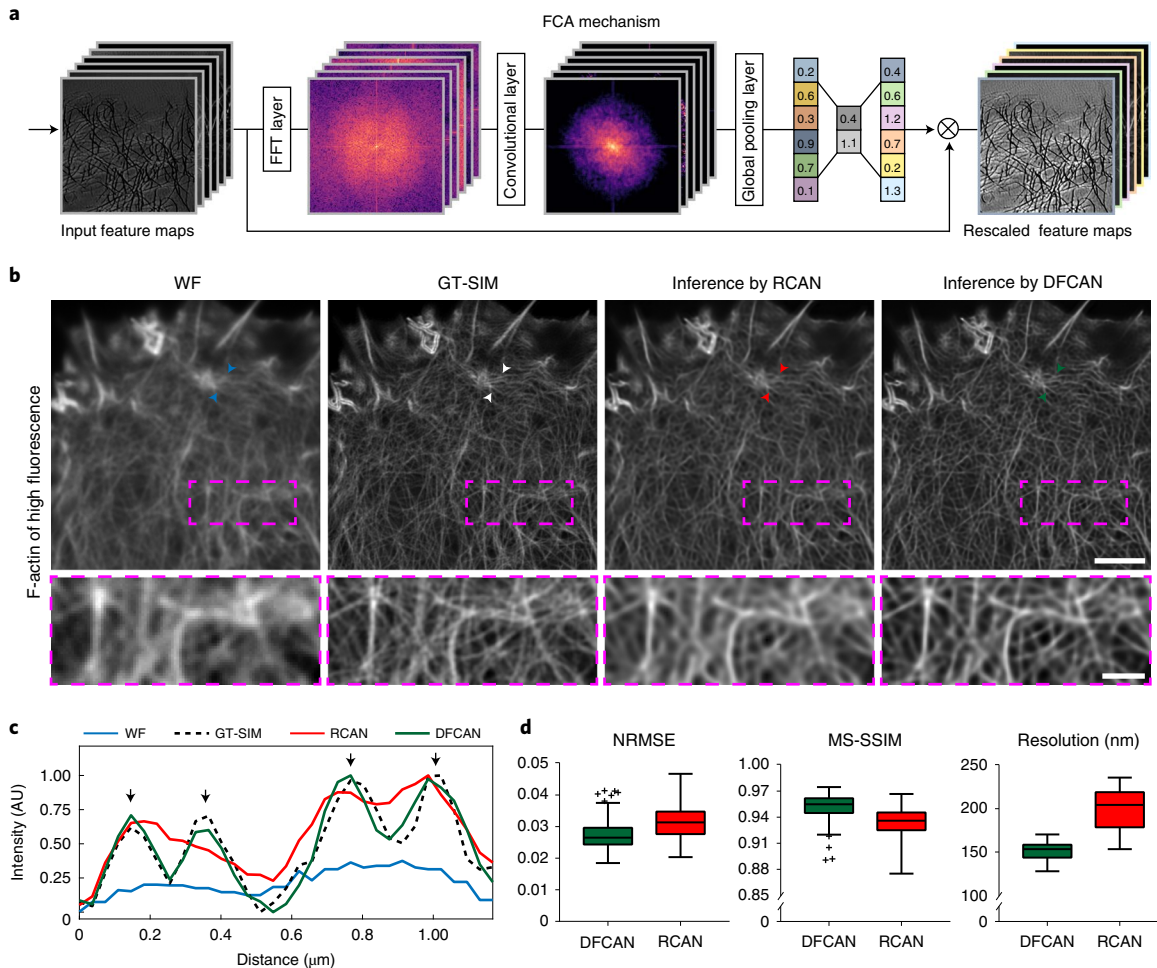


Fig. 2 | FCA mechanism and comparison of SISR images via DFCAN and RCAN. **a**, Schematic of the FCA mechanism. **b**, Comparison of SISR images of F-actins inferred by DFCAN and RCAN. WF and GT-SIM images are shown for reference. Lower row shows the magnified images of the boxed regions in the upper images. Scale bar, 3 μm ; 1 μm for magnified images. Gamma values, 0.8. Experiments were repeated with 117 images, achieving similar results. **c**, Intensity profiles along the lines indicated by the arrowheads in the images of WF (blue), GT-SIM (white), DFCAN (green) and RCAN (red). **d**, Statistical comparison of DFCAN and RCAN in terms of NRMSE, MS-SSIM and resolution, $n=117$. Tukey box-and-whisker plots with outliers displayed as black crosses are shown (Methods). AU, arbitrary units.

and reconstructed into an SR-SIM image. The WF images were used as the input LR images for the DLSR networks, whereas the SIM images served as the reference to assess whether the DLSR methods outperformed conventional SR microscopy under specific imaging conditions. In this way, all of the LR-SR image pairs are well matched and there is no need for registration.

Evaluation of representative DLSR models. Here, we selected four representative DLSR models constructed with different network architectures (Supplementary Note 1), including an SR convolutional neural network (SRCNN)¹—the earliest SR network with a lightweight configuration; an enhanced deep SR (EDSR) network²—a recent development in deep CNNs constructed with residual convolutional blocks to achieve greatly expanded network depth; image-to-image translation with a conditional GAN (termed Pix2Pix)¹⁷; and the cross-modality GAN (CMGAN)¹¹.

Figure 1a and Extended Data Fig. 2 show the SISR images inferred from single WF images of high and medium fluorescence levels, respectively. Compared with the input WF images, the SISR images present amounts of structures finer than the diffraction-limited scale, such as the hollow, ring-like structure of CCPs and the network of crisscrossing MT or F-actin filaments, etc. To visualize the defects

of these SISR images directly, we computed the pixelwise absolute difference between the SISR images and the corresponding ground truth SIM (GT-SIM) images. The difference images illustrate that a medium or relatively high fluorescence signal level, which is typical for live-cell SIM imaging¹³, is sufficient to permit conventional SIM generally outperforming current DLSR approaches, although the overall morphology of the biological structures shown in the SISR images is similar to that in the GT-SIM images (Supplementary Videos 1–5). In contrast, under imaging conditions of low fluorescence (Fig. 1b), SISR images show less residual difference than conventional SIM images, because data-driven DLSR approaches are usually conducive to separating noise from biological structures¹⁰. Nonetheless, if the desired upscaling factor increases to 3 \times , the SISR images (bottom rows of Fig. 1a,b) will contain too many errors or artifacts to allow one to trust the fine structures inferred.

To evaluate the performance of different SR methods quantitatively, we integrated the three metrics of the normalized root-mean-square error (NRMSE), multiscale structural similarity index (MS-SSIM) and resolution to measure the quality of an SR image for each imaging condition in the assessment matrix (Methods; Supplementary Notes 2–4). Because scientific research generally demands highly faithful and quantifiable SR images at the

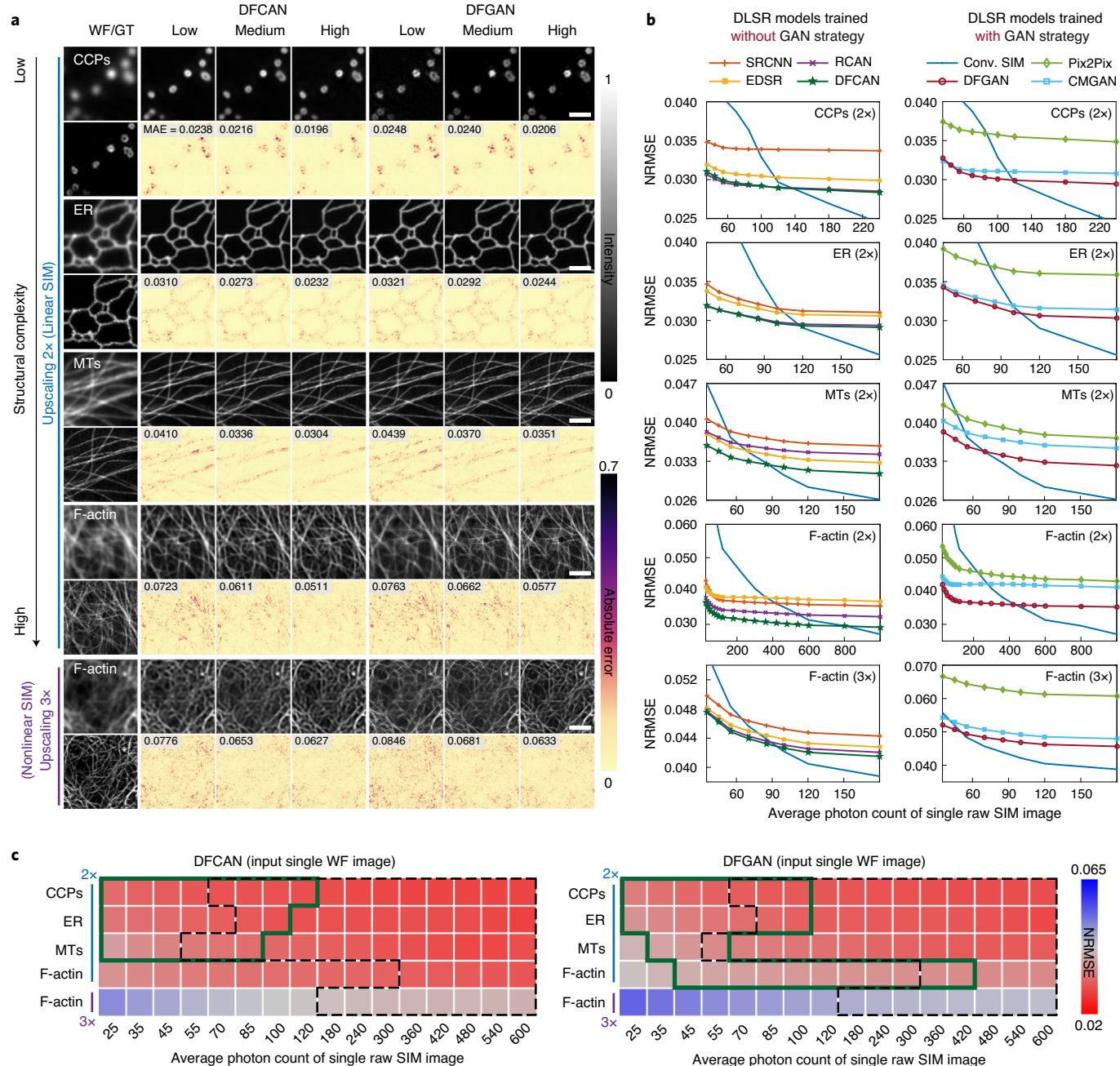


Fig. 3 | Characterization of DFCAN and DFGAN. **a**, Representative SISR images inferred by DFCAN or DFGAN from low (left), medium (middle) and high (right) fluorescence WF images of the same ROIs as in Fig. 1a,b. Scale bar, 0.75 μm for CCPs; 1.5 μm for other specimens. **b**, NRMSE comparisons of the seven DLSR models that are classified into two categories: non-GAN models (left) and GAN-based models (right) in the cases of CCPs, ER, MTs and F-actin (upsampling 2x), and F-actin (upsampling 3x). **c**, Assessment matrices of DFCAN- and DFGAN-SISR in terms of NRMSE illustrating their priority regions (green) and the applicable region of Conv. SIM (dashed black). Gamma values, 0.6 for the F-actin images of upscaling 3x in **a**.

expense of fluorescence photons, we first identified the applicable region of conventional SIM in the space of the assessment matrix (outlined by dashed black line in Fig. 1c), where the three metrics of the conventional SIM images were close to those of the GT (Supplementary Fig. 3 and Note 4). The applicable region of conventional SIM covers mainly regions of medium- or high fluorescence, consistent with the practical conditions used in live-cell SIM imaging experiments.

Additionally, the three metrics were utilized to evaluate the four DLSR models and generate their assessment matrices (Fig. 1c and Supplementary Figs. 4–7). According to the evaluation, we defined

the priority region for using a DLSR model, where the three metrics of the SISR image were comparable with or better than those of the conventional SIM image (outlined in green in Fig. 1c and Supplementary Note 4). Clearly, the larger the priority region, the better the performance of a DLSR model. However, it is noteworthy that the priority regions of all four DLSR models are relatively small and concentrate on zones of low fluorescence and low structural complexity, which rarely overlap with the applicable region of conventional SIM (Fig. 1c). These data suggest that hardware SR microscopy, for example, SIM, utilizes the increased fluorescence more efficiently than state-of-the-art DLSR models to generate

high-fidelity SR information, which may impede the widespread application of DLSR models in practical experiments.

Deep Fourier channel attention networks. After learning the properties of the current DLSR models, we devised DFCAN and DFGAN (Extended Data Fig. 3 and Methods), which exploit the characteristics of the power spectrum of distinct feature maps in the Fourier domain. In each residual block, the Fourier channel attention (FCA) mechanism (Fig. 2a) enables the network to adaptively rescale each feature map according to the integrated contributions from all frequency components contained in its power spectrum (Supplementary Note 5). In contrast, the spatial channel attention (SCA) mechanism utilizes only the average intensity of the feature maps, which is equivalent to the zero frequency (that is, DC component), to compute the rescaling factors^{5,15}.

To test whether FCA outperforms SCA in the SISR task, we implemented the FCA and SCA mechanisms, respectively, in different network architectures of ResNet⁵, U-net¹⁸ and DenseNet¹⁹. We found that the FCA-based networks generally provided less NRMSE and inferred the fine structures more precisely than the corresponding networks based on SCA (Extended Data Fig. 4 and Methods). Moreover, we demonstrate that although DFCAN has sevenfold fewer parameters than RCAN (Supplementary Table 1), DFCAN more precisely resolves the densely crisscrossing regions of F-actin cytoskeleton (Fig. 2b), and the line-scan profiles of F-actins from the DFCAN images are closer to the profiles of GT-SIM than those from the RCAN images (Fig. 2c). The statistical analysis quantified that DFCAN typically achieved better DLSR imaging performance in terms of all three metrics, especially for the high-structural-complexity specimens, for example, MTs and F-actin (Fig. 2d and Supplementary Tables 2–4).

Furthermore, we systematically evaluated the SR imaging performance of RCAN, DFCAN and DFGAN with the same metrics used for the other DLSR models (Supplementary Figs. 8–10). As shown in Fig. 3a, the SISR images inferred by DFCAN or DFGAN generally exhibit less residual difference than the corresponding images inferred by other DLSR models (Supplementary Videos 1–5). To illustrate clearly the performance difference among all evaluated DLSR models, we classified them into two categories: non-GAN and GAN-based models. For each type of specimen, we plotted the NRMSE, MS-SSIM and resolution of the same category models as a function of fluorescence intensity, respectively (Fig. 3b and Extended Data Fig. 5). These results reveal that the NRMSE of either DFCAN or DFGAN is generally smaller than that of the other DLSR models from the same category. More importantly, in terms of the NRMSE and MS-SSIM metrics, conventional SIM could not surpass DFCAN and DFGAN until relatively high fluorescence was reached. Consequently, both DFCAN and DFGAN afford enlarged priority regions relative to other DLSR models (Fig. 3c).

SISR live-cell imaging via DFCAN and DFGAN. Next, we tested whether DFCAN and DFGAN were competent in the SISR live-cell imaging task with 2 \times upscaling. Mitochondria are highly dynamic organelles that contain multiple nucleoids and exquisite cristae-like inner membrane invaginations. Mitochondrial dynamics are important for the maintenance of mitochondrial functions and for cellular quality control²⁰. However, it remains challenging to achieve long time-lapse SR imaging of mitochondrial dynamics, because current SR imaging techniques demand high illumination intensity and/or a long exposure time to acquire multiple raw images^{21,22}, which are prone to causing phototoxicity in mitochondria²³. Thus far, little is known about how the locations and movements of nucleoids are regulated within the ultrastructure of the mitochondrial inner membrane.

In this work, we applied DFCAN- and DFGAN-SISR live-cell imaging to characterize the dynamics of nucleoids in terms of

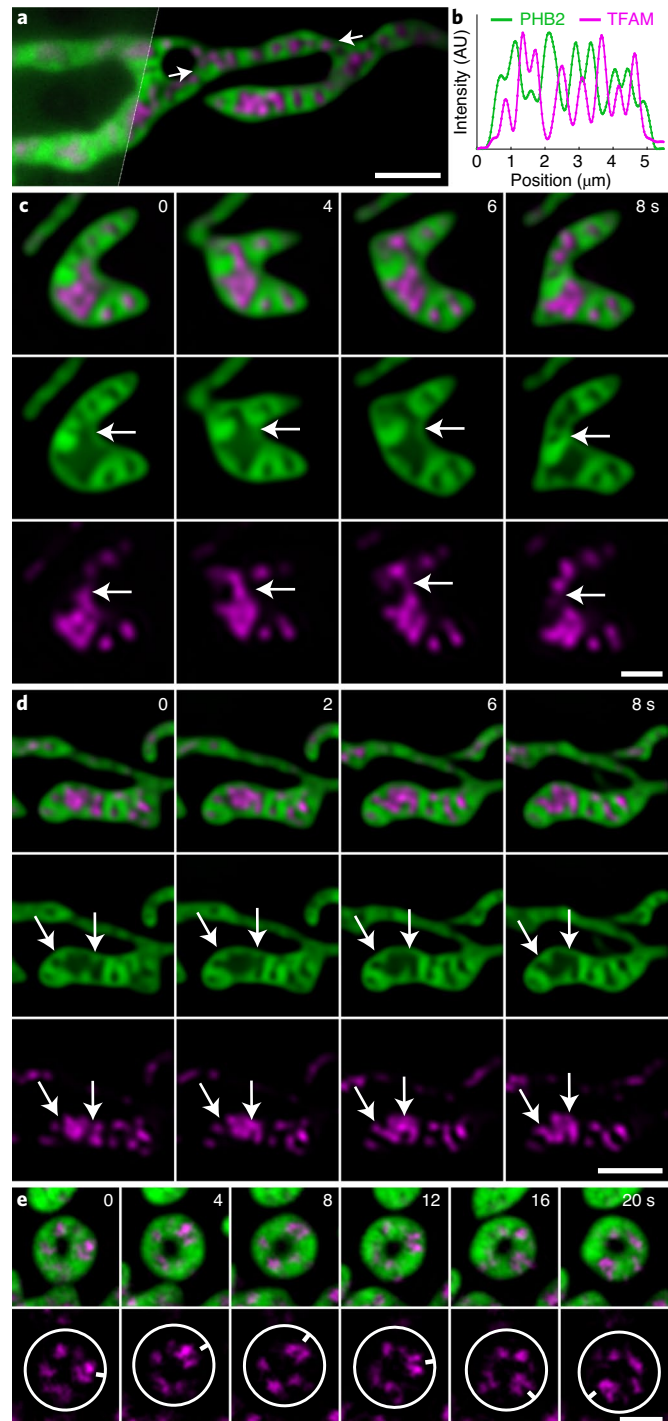


Fig. 4 | Live-cell SISR imaging via DFCAN and DFGAN. **a**, Representative two-color DFCAN-SISR images of mitochondrial inner membrane (green) and nucleoids (magenta) from COS-7 cells expressing mEmerald-PHB2 and mCherry-TFAM simultaneously. Top left: a fraction of the corresponding WF image. **b**, Intensity profiles of cristae (green) and nucleoids (magenta) along the line indicated by the arrows in **a**. **c**, Time-lapse DFCAN-SISR images of a typical nucleoid fission event concomitant with the formation of a new cristae in between. **d**, Time-lapse DFCAN-SISR images of a typical nucleoid fusion event concomitant with the recession of the intermediate cristae. **e**, Time-lapse DFGAN-SISR images illustrating the bidirectional rotation of circular mitochondrial tubes. The lower row shows that nucleoids change their orientation accordingly. Scale bar, 2 μ m (**a,d**); 1 μ m (**c,e**). Gamma values: 0.85 for TFAM channel in all images. Experiments were repeated independently for $n=10$ COS-7 cells, all showing similar characteristics and performance.

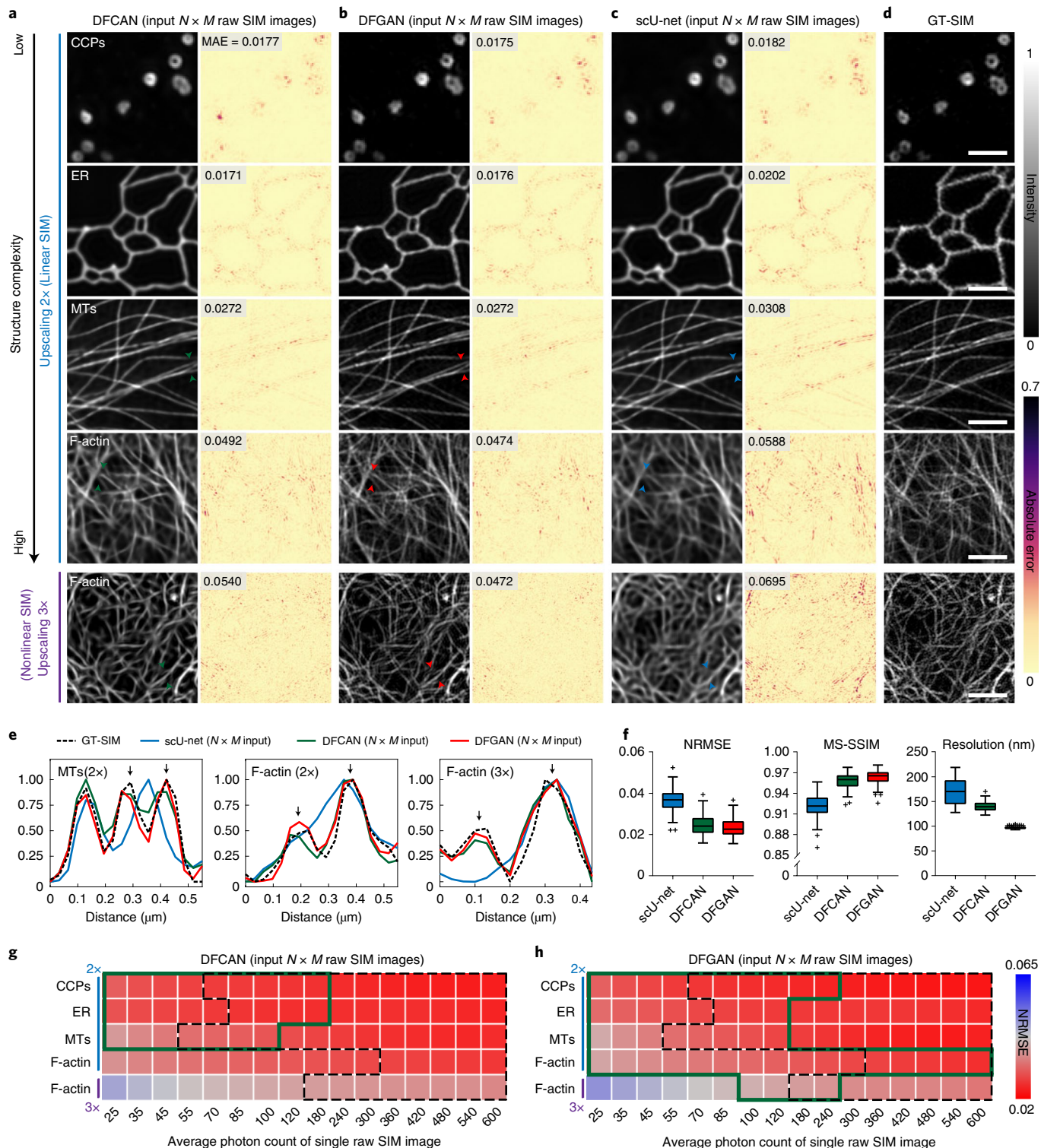


Fig. 5 | Comparison of SIM reconstruction via DFCAN, DFGAN and scU-net. **a–c**, Representative SR images reconstructed by DFCAN (**a**), DFGAN (**b**) and scU-net (**c**) from linear-SIM raw images of CCPs, ER, MTs and F-actin (first to fourth row), and nonlinear SIM raw images of F-actin (fifth row). **d**, The corresponding GT-SIM images. Scale bar, 0.75 μm for CCPs; 1.5 μm for other specimens. **e**, Intensity profiles of MTs, F-actin (2 \times and 3 \times upscaling) along the lines indicated by the two arrowheads in the images of (**a**) DFCAN (green), (**b**) DFGAN (red), (**c**) scU-net (blue) and (**d**) GT-SIM (dashed black). The arrows indicate that the structures reconstructed by DFCAN or DFGAN are closer to GT-SIM than those reconstructed by scU-net. **f**, Statistical comparison of scU-net, DFCAN and DFGAN in terms of NRMSE, MS-SSIM and resolution for F-actin (2 \times upscaling), $n=121$. Tukey box-and-whisker plots with outliers displayed as black crosses are shown (Methods). **g,h**, Assessment matrices of DFCAN-SIM (**g**) and DFGAN-SIM (**h**) in terms of NRMSE, illustrating their priority regions (green) and the applicable region of Conv. SIM (dashed black). Gamma values: 0.6 for F-actin image of 3 \times upscaling in **a–d**.

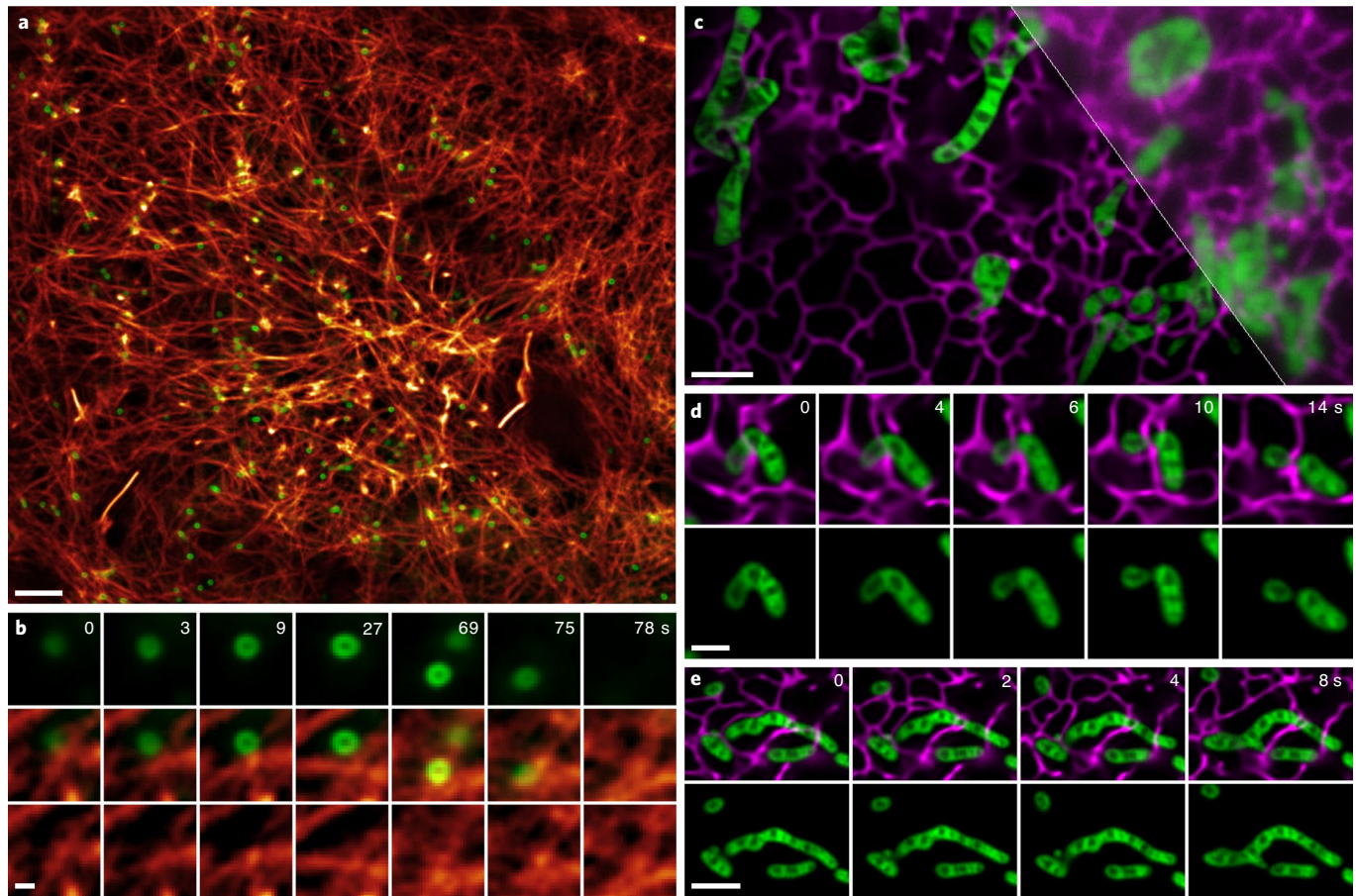


Fig. 6 | Two-color SR live-cell imaging by DFCAN- and DFGAN-SIM. **a**, Representative SR images of F-actin (red, reconstructed by DFGAN-SIM) and CCPs (green, reconstructed by DFCAN-SIM) in live COS-7 cells. **b**, Time-lapse images showing the interactions of F-actin and CCPs during endocytosis. **c**, Representative SR images of ER (magenta) and mitochondrial cristae (green) generated by the transfer-learned models of DFCAN-SIM and DFGAN-SIM, respectively. Top right: a fraction of the corresponding WF image averaged from raw SIM images. **d,e**, Time-lapse images showing mitochondrial fission (**d**) and fusion (**e**) events occurring at ER-mitochondria contact sites. Scale bar, 2 μm (**a,c**), 0.2 μm (**b**), 1 μm (**d**), 2 μm (**e**). Gamma values, 0.85 for F-actin channel in (**a,b**); 0.8 for ER channel in (**c**). Experiments were repeated independently for $n=10$ COS-7 cells, all showing similar characteristics and performance.

mitochondrial cristae deformation. As shown in Fig. 4a, DFCAN-SISR two-color imaging reveals that mitochondrial cristae are often arranged into groups that are interspaced by multiple nucleoids (Fig. 4b), which is consistent with the results obtained by conventional SIM and stimulated emission depletion (STED) microscopy^{13,21}. Since the acquisition of a single WF image for DFCAN requires much less fluorescence than conventional SR approaches (Methods), DFCAN-SISR permits long time-lapse SR live-cell imaging over 1,000 frames, which extends the imaging duration by ~tenfold compared with conventional SIM or STED microscopy^{13,21,22}. Thus, it allows continuous capture of the reorganization of nucleoids during the mitochondrial membrane dynamics of dividing, coalescing and cristae deformation (Supplementary Video 6). Interestingly, we observed that the partitioning of a large nucleoid was concomitant with the protrusion of the nearby cristae (arrows in Fig. 4c); moreover, the coalescing of two adjacent nucleoids was coincident with the recession of intermediate cristae (arrows in Fig. 4d). These observations suggest that the dynamic reorganization of mitochondrial cristae might facilitate the fission and fusion of nucleoids, and hence regulate the distribution of nucleoids within mitochondria.

In addition, DFGAN-SISR revealed that most of the circular mitochondrial tubes underwent bidirectional rotation at an angular velocity of $7.2 \pm 6.7^\circ$ per second (Fig. 4e and Supplementary Video 7), which was presumably propelled by hydrodynamic forces

generated by cytoplasmic streaming²⁴. This result indicates that not only large plant cells but also relatively small animal cells are capable of generating spiral rotational streaming to facilitate the circulation of intracellular contents to maintain the homeostasis of the intracellular environment. Finally, all of the aforementioned biological processes have been verified with a conventional GI-SIM system (Extended Data Fig. 6), which confirms the usability of DFCAN and DFGAN in practical experiments.

SIM image reconstruction via DFCAN and DFGAN. SIM has become increasingly popular for SR live-cell imaging²⁵, but it necessitates computational reconstruction that is prone to introducing artifacts to the SR-SIM images under imaging conditions of low SNR or high out-of-focus background²⁶. Here, we exploited the FCA's advantage of modeling the interdependencies between informative feature maps in the Fourier domain to achieve robust high-quality reconstruction of SIM images.

Instead of entering a single WF image, both DFCAN and DFGAN were reconfigured to accept raw SIM images of the N -phase by M -orientation and output a single SR image (Methods). As shown in Fig. 5a,b, the representative DFCAN- and DFGAN-SIM images are fairly close to the GT-SIM images, although the fluorescence of its raw images is ~tenfold lower than that of GT-SIM (Fig. 5d). At a relatively low fluorescence level, compared with previous

denoising methods for SR imaging, for example, Hessian-SIM²⁷, DFCAN and DFGAN are able to reconstruct more HR structures while suppressing artifacts (Extended Data Fig. 7). Moreover, we demonstrate that DFCAN and DFGAN offer high robustness to reconstruct high-quality SR images from the simulated data of high background, and from experimental data acquired without total internal reflection fluorescence (TIRF) illumination (Extended Data Fig. 8).

Furthermore, compared with the recent U-net model that was also developed for SIM reconstruction (termed scU-Net)²⁸, DFCAN- and DFGAN-SIM produce SR images of less residual difference (Fig. 5a,b versus Fig. 5c). As exemplified in Fig. 5e, the line-scan profiles from DFCAN-SIM and DFGAN-SIM images are mostly equivalent to those of GT-SIM. However, the profiles plotted from scU-Net SIM images usually deviate from those of GT-SIM and may even fail to resolve the adjacent F-actin filaments (indicated by the arrows in Fig. 5e). The statistical analysis of more than 100 sets of F-actin data confirms that both DFCAN- and DFGAN-SIM significantly outperform scU-Net in terms of all three metrics (Fig. 5f). Additionally, we demonstrate that DFCAN and DFGAN can be extended for 3D-SIM reconstruction, which successfully improves the volumetric resolution and eliminates the out-of-focus background for diverse specimens (Supplementary Fig. 11 and Note 6).

Finally, for each type of specimen, we quantified the performance of these DLSR models by calculating the three metrics of NRMSE, MS-SSIM and resolution (Extended Data Fig. 9 and Supplementary Tables 2–4). It can be seen that DFCAN-SIM and DFGAN-SIM perform better than DFCAN-SISR and DFGAN-SISR, respectively, at all fluorescence levels, suggesting that the Moiré patterns encoded in raw SIM images are helpful for the network in restoring valuable high-frequency information. Therefore, the priority region of DFCAN-SIM and DFGAN-SIM was extended to cover more imaging conditions in the assessment matrices (Fig. 5g,h) than other DLSR models.

DFCAN- and DFGAN-SIM live-cell imaging of organelle and cytoskeletal interactions. It has been shown that the actin cytoskeleton is involved in regulating clathrin-mediated endocytosis (CME)²⁹, but it remains unclear how the dynamics of the actin filaments influence the CME process. To investigate the interaction dynamics over an extended timecourse, we acquired raw SIM images of ~tenfold less fluorescence than that of GT-SIM. Despite the relatively low fluorescence, DFCAN- and DFGAN-SIM still prevents the generation of reconstruction artifacts, and resolves successfully the ring structures of the CCPs and the fine branches of actin filaments for more than 400 timepoints (Fig. 6a and Supplementary Video 8). Interestingly, we found that most CCPs were initiated within the tiny voids interspersed throughout the vast network of actin filaments, and then grew into hollow ring structures gradually without frequent interactions with adjacent actin filaments (Fig. 6b, 0–27 s). In contrast, immediately before the pits detached from the cell membrane, we observed intensive contact between actin filaments and CCPs (Fig. 6b, 69–75 s), suggesting that actin filaments might facilitate the internalization of CCPs in the late stage of endocytosis.

Given the large diversity of biological structures, it is difficult to obtain sufficient high-quality training datasets for every structure. Transfer learning strategies have been commonly employed to repurpose a pretrained network for other related tasks³⁰. To assess the transfer learning potential of DFCAN and DFGAN, we employed the prelearned DFCAN- or DFGAN-SIM model with F-actin data as the initial model to speed up the training process for the CCPs, ER, MTs and mitochondrial inner membrane (Supplementary Note 7). After transfer learning, most of the typical features beyond diffraction-limited scale were resolved as clearly as those resolved by the corresponding models trained with matched datasets (Extended Data Fig. 10 and Supplementary Fig. 12).

Subsequently, we applied the transfer-learned DFGAN-SIM model of mitochondria and DFCAN-SIM model of ER to characterize their dynamic interactions in live cells. A representative two-color frame from a long time-lapse movie of 421 timepoints (Fig. 6c and Supplementary Video 9) shows that ER-mitochondria contacts not only exist commonly but are also retained through the constant activities of mitochondrial writhing and deformation. Moreover, we found that mitochondrial dividing and coalescing loci were often defined by the contact sites of mitochondria and ER tubules (Figs. 6d,e), and the subtle yet dynamic deformations of mitochondrial cristae were resolved clearly during the progression of division and coalescence (arrows in Supplementary Video 10). These results demonstrate that DFCAN and DFGAN algorithms lay the groundwork for opening up a wider application range of SIM live-cell imaging.

Discussion

In this work, we first provided an open-access experimental dataset, BioSR, that consists of extensive LR-SR image pairs covering wide ranges of SNR levels, structural complexity and upscaling factors. Currently, simulated datasets that assume simple and uniform degradation are commonly used to train and assess DLSR models^{1–5,31}, but recent work⁷ has demonstrated that DLSR models trained with simulated data actually do not show the expected high performance in real applications, presumably because the degradation process in the real world is more complicated than that in simulation⁷. The BioSR dataset provides a high-quality benchmark for evaluating the fidelity and quantifiability of current and future DLSR networks, which is crucial for applications involving largely the quantitative analysis of image data.

To further improve DLSR imaging performance, we devised the DFCAN and DFGAN architectures, which leverage the frequency content difference across distinct features to adaptively rescale their weightings when propagating them through the network. This strategy enables the network to learn precise hierarchical mappings from LR to SR images. We believe that the concept of DFCAN and DFGAN has great potential to advance other image transformation tasks, in which the content difference between network inputs and outputs when presented in another specific domain is more prominent than that in their original domain.

Moreover, DFCAN and DFGAN enabled investigation of the fragile biological processes that are challenging for conventional SR microscopy. For instance, among other achievements, DFCAN-SISR first revealed that the partitioning and coalescing of mitochondrial nucleoids was regulated delicately by the protrusion and recession of neighboring cristae, respectively. These results demonstrate the potential of DFCAN and DFGAN to advance the performance of existing SR microscopy.

Furthermore, we noted that GAN-based models (for example, DFGAN and CMGAN) typically offer HR close to GT-SIM, but their NRMSE and MS-SSIM are usually worse than that of non-GAN models (for example, DFCAN and RCAN). This suggests that non-GAN models are more applicable to low- to medium-fluorescence imaging conditions to generate SR images of good quantifiability. However, if a GAN model is able to offer comparable NRMSE and MS-SSIM to conventional SIM (for example, DFGAN), it will be the preferred DLSR model, especially for high-structural complexity specimens.

Despite the impressive results of current DLSR models, it is noteworthy that image transformation is essentially an ill-posed problem⁶. This indicates that, although deep-learning models leverage a large amount of well-registered data to learn good statistical transformation, it is theoretically impossible for network inference to obtain GT images in every detail. As revealed in this work, regardless of which DLSR model is used, both assessment functions of the NRMSE and MS-SSIM versus fluorescence intensity quickly approach asymptotic stability but cannot reach ideal values even

when approaching infinite fluorescence. In contrast, the metrics of conventional SIM images increasingly approach deal values as the fluorescence intensity approaches the GT imaging level. Therefore, this limitation indicates the great challenge of fully replacing the SR microscope with computational-only approaches. In our opinion, a holistic design that wisely integrates deep-learning algorithms into the development of microscope hardware might be a promising approach in next-generation SR microscopy.

Online content

Any methods, additional references, Nature Research reporting summaries, source data, extended data, supplementary information, acknowledgements, peer review information; details of author contributions and competing interests; and statements of data and code availability are available at <https://doi.org/10.1038/s41592-020-01048-5>.

Received: 15 April 2020; Accepted: 11 December 2020;

Published online: 21 January 2021

References

- Dong, C., Loy, C. C., He, K. & Tang, X. Image super-resolution using deep convolutional networks. *IEEE Trans. Pattern Anal. Mach. Intell.* **38**, 295–307 (2016).
- Lim, B., Son, S., Kim, H., Nah, S. & Mu Lee, K. Enhanced deep residual networks for single image super-resolution. In *Proc. IEEE Conference on Computer Vision and Pattern Recognition Workshops* (eds. Chellappa, R. et al.) 1132–1140 (IEEE, 2017).
- Lai, W.-S., Huang, J.-B., Ahuja, N. & Yang, M.-H. Deep Laplacian pyramid networks for fast and accurate super-resolution. In *Proc. IEEE Conference on Computer Vision and Pattern Recognition* (eds. Chellappa, R. et al.) 624–632 (IEEE, 2017).
- Ledig, C. et al. Photo-realistic single image super-resolution using a generative adversarial network. In *Proc. IEEE Conference on Computer Vision and Pattern Recognition* (eds. Chellappa, R. et al.) 4681–4690 (IEEE, 2017).
- Zhang, Y. et al. Image super-resolution using very deep residual channel attention networks. In *Proc. European Conference on Computer Vision (ECCV)* (eds. Ferrari, V. et al.) 286–301 (Springer, 2018).
- Yang, W. et al. Deep learning for single image super-resolution: a brief review. *IEEE Trans. Multimed.* **21**, 3106–3121 (2019).
- Cai, J., Zeng, H., Yong, H., Cao, Z. & Zhang, L. Toward real-world single image super-resolution: a new benchmark and a new model. In *Proc. IEEE International Conference on Computer Vision* (eds. Davis, L. S. et al.) 3086–3095 (IEEE, 2019).
- Cai, J., Gu, S., Timofte, R. & Zhang, L. Ntire 2019 challenge on real image super-resolution: methods and results. In *Proc. IEEE Conference on Computer Vision and Pattern Recognition Workshops* (eds. Brown, M. S. et al.) 2211–2223 (IEEE, 2019).
- Lugmayr, A., Danelljan, M. & Timofte, R. NTIRE 2020 challenge on real-world image super-resolution: methods and results. In *Proc. IEEE/CVF Conference on Computer Vision and Pattern Recognition Workshops* (Boult, T. T. et al.) 494–495 (IEEE, 2020).
- Weigert, M. et al. Content-aware image restoration: pushing the limits of fluorescence microscopy. *Nat. Methods* **15**, 1090–1097 (2018).
- Wang, H. et al. Deep learning enables cross-modality super-resolution in fluorescence microscopy. *Nat. Methods* **16**, 103–110 (2019).
- Belthangady, C. & Royer, L. A. Applications, promises, and pitfalls of deep learning for fluorescence image reconstruction. *Nat. Methods* **16**, 1215–1225 (2019).
- Guo, Y. et al. Visualizing intracellular organelle and cytoskeletal interactions at nanoscale resolution on millisecond timescales. *Cell* **175**, 1430–1442 e1417 (2018).
- Li, D. et al. Extended-resolution structured illumination imaging of endocytic and cytoskeletal dynamics. *Science* **349**, aab3500 (2015).
- Hu, J., Shen, L. & Sun, G. Squeeze-and-excitation networks. In *Proc. IEEE Conference on Computer Vision and Pattern Recognition* (eds. Brown, M. S. et al.) 7132–7141 (IEEE, 2018).
- Gustafsson, M. G. et al. Three-dimensional resolution doubling in wide-field fluorescence microscopy by structured illumination. *Biophys. J.* **94**, 4957–4970 (2008).
- Isola, P., Zhu, J.-Y., Zhou, T. & Efros, A. A. Image-to-image translation with conditional adversarial networks. In *Proc. IEEE Conference on Computer Vision and Pattern Recognition* (eds. Chellappa, R. et al.) 1125–1134 (IEEE, 2017).
- Ronneberger, O., Fischer, P. & Brox, T. U-Net: Convolutional networks for biomedical image segmentation. In *Proc. International Conference on Medical Image Computing and Computer-Assisted Intervention* (eds Navab, N. et al.) 234–241 (Springer, 2015).
- Huang, G., Liu, Z., Van Der Maaten, L. & Weinberger, K. Q. Densely connected convolutional networks. In *Proc. IEEE Conference on Computer Vision and Pattern Recognition* (eds. Chellappa, R. et al.) 4700–4708 (IEEE, 2017).
- Westermann, B. Mitochondrial fusion and fission in cell life and death. *Nat. Rev. Mol. Cell Biol.* **11**, 872–884 (2010).
- Stephan, T., Roesch, A., Riedel, D. & Jakobs, S. Live-cell STED nanoscopy of mitochondrial cristae. *Sci. Rep.* **9**, 12419 (2019).
- Shim, S. H. et al. Super-resolution fluorescence imaging of organelles in live cells with photoswitchable membrane probes. *Proc. Natl Acad. Sci. USA* **109**, 13978–13983 (2012).
- Wang, C. et al. A photostable fluorescent marker for the superresolution live imaging of the dynamic structure of the mitochondrial cristae. *Proc. Natl Acad. Sci. USA* **116**, 15817–15822 (2019).
- Goldstein, R. E., Tuval, I. & van de Meent, J.-W. Microfluidics of cytoplasmic streaming and its implications for intracellular transport. *Proc. Natl Acad. Sci. USA* **105**, 3663–3667 (2008).
- Wu, Y. & Shroff, H. Faster, sharper, and deeper: structured illumination microscopy for biological imaging. *Nat. Methods* **15**, 1011–1019 (2018).
- Li, D. & Betzig, E. Response to Comment on “Extended-resolution structured illumination imaging of endocytic and cytoskeletal dynamics”. *Science* **352**, 527–527 (2016).
- Huang, X. et al. Fast, long-term, super-resolution imaging with Hessian structured illumination microscopy. *Nat. Biotechnol.* **36**, 451–459 (2018).
- Jin, L. et al. Deep learning enables structured illumination microscopy with low light levels and enhanced speed. *Nat. Commun.* **11**, 1934 (2020).
- Collins, A., Warrington, A., Taylor, K. A. & Svitkina, T. Structural organization of the actin cytoskeleton at sites of clathrin-mediated endocytosis. *Curr. Biol.* **21**, 1167–1175 (2011).
- Burke, L. A. & Hutchins, H. M. Training transfer: an integrative literature review. *Hum. Resour. Dev. Rev.* **6**, 263–296 (2007).
- Christensen, C. N., Ward, E. N., Lio, P. & Kaminski, C. F. ML-SIM: a deep neural network for reconstruction of structured illumination microscopy images. Preprint at <https://arxiv.org/abs/2003.11064> (2020).

Publisher's note Springer Nature remains neutral with regard to jurisdictional claims in published maps and institutional affiliations.

© The Author(s), under exclusive licence to Springer Nature America, Inc. 2021

Methods

Multimodality structured illumination microscopy. The multimodality SIM system was developed from our previous GI-SIM and TIRF-SIM setups¹³. Briefly, three laser beams of 405 nm (LBX-405-300, Oxxius), 488 nm (Genesis-MX-SLM, Coherent) and 560 nm (2RU-VFL-P-500-560, MPB Communications) were combined collinearly, and then passed through an acousto-optic tunable filter (AOTF, AOTFnC-400.650, AA Quanta Tech). According to the demands of the specific imaging mode, the AOTF could control the exposure sequence and duration of the desired laser beams flexibly. The selected laser light was then expanded and sent into an illumination pattern generator, which is composed of a ferroelectric spatial light modulator (SLM, QXGA-3DM, Forth Dimension Display), a polarization beam splitter and an achromatic halfwave plate. Depending on the exposure design of the specific imaging mode, the pattern generator could program the display sequence and duration of given grating patterns synergizing with the laser light selected by the AOTF. Light diffracted by the grating pattern was passed through a polarization rotator consisting of a liquid crystal cell (Meadowlark, LRC-200) and quarterwave plate, which rotated the linear polarization of diffracted light according to the orientation of ± 1 diffraction orders, so as to maintain the *s*-polarization necessary to maximize the pattern contrast for all pattern orientations. The high diffraction orders, except for ± 1 orders, were filtered out by a spatial mask, and then the ± 1 orders light was relayed onto the back focal plane of a high numerical aperture (NA) objective (APON100XHOTIRF 1.7 NA, Olympus). The distance and orientation of the $+1$ and -1 order light spots could be adjusted by changing the period and orientation of the pattern displayed on the SLM, so that the high NA TIRF-SIM and relatively low NA GI-SIM illumination of three-phase \times three-orientation, as well as nonlinear SIM of five-phase \times five-orientation under TIRF or GI illumination could be deployed in the same system. The raw SIM images excited sequentially by different illumination patterns were collected by the same objective, then separated by a dichroic mirror (Chroma, ZT405/488/560/647tpc) and finally relayed onto a scientific complementary metal oxide semiconductor (sCMOS) camera (Hamamatsu, Orca Flash 4.0 v.3). The 9 raw images of TIRF-SIM or GI-SIM, and 25 raw images of nonlinear SIM were reconstructed into SR images of twofold and threefold resolution improvement, respectively, using the previous algorithm^{13,14,16}. To minimize the reconstruction artefacts of SIM images acquired at low- or medium-fluorescence intensity level, we applied a Gaussian apodization function, whose cutoff frequency matched the boundary of reconstructed optical transfer function (OTF) to suppress the noise in the high-frequency region.

Training and test data acquisition. For each type of specimen and each imaging modality, we acquired the raw datasets from at least 50 distinct regions-of-interest (ROI), from which the datasets of 35 ROIs were used for training while the datasets of the other 15 ROIs were used to generate the assessment matrices.

For each ROI, we acquired nine sets of N -phase $\times M$ -orientation raw images with constant 1 ms exposure time but increasing the excitation light intensity, where N and M are three for TIRF-SIM and GI-SIM, and five for nonlinear SIM. Each set of $N \times M$ raw images were averaged as a diffraction-limited WF image, which are then masked to calculate its average photon count per pixel. The raw SIM images and WF images of different fluorescence levels were used as the input LR image for DLSR networks. Meanwhile, each set of $N \times M$ raw images was reconstructed into a SIM image attributing the same fluorescence level as the corresponding WF image, which served as a reference to assess the quality of the DLSR image at that fluorescence level. In addition, in the same ROI, we finally elevated the excitation intensity and exposure time (typically 120 W cm^{-2} for 10 ms) to achieve a high fluorescence level of $>1,200$ average photon count, and independently acquired three sets of $N \times M$ raw images. The resulting three SIM images of ultrahigh SNR were averaged as the GT-SIM image to guarantee high quality.

Evaluation of the DLSR model demands well-matched LR-SR image pairs, so the cells were fixed 16–36 h post-transfection to acquire data for CCPs, MTs and F-actin. However, we found that current chemical fixation methods cause obvious aggregations of our ER marker protein calnexin that significantly change ER morphology relative to live status, so we acquired ER data from live cells. To reduce the influence of sample motion and allow the LR and SR images of ER to match each other as much as possible, we acquired a single GT-SIM image for each fluorescence level. Each raw SIM image was collected under the imaging condition of 5 ms at 200 W cm^{-2} . Although this imaging condition is a balanced option in terms of SNR and sample motion, we have to apply a relatively stringent Gaussian apodization function ($\sigma = 47 \text{ nm}$, that is, $21.3 \mu\text{m}^{-1}$) to minimize the residual sample motion-induced artifacts, which compromised the resolution of GT-SIM images of ER to $145.1 \pm 6.5 \text{ nm}$. Otherwise, sample motion artifacts would be learned by the DLSR models, especially GAN-based ones, and represented on their inference.

On the other hand, we found that transiently transfected clathrin-SkylanNS and enconsin-SkylanNS commonly showed high cytoplasm background fluorescence superposed onto the structures of CCPs and MTs. The contrast of raw images was not good enough to reconstruct high quality GT nonlinear SIM images of CCPs and MTs. Therefore, we evaluated DLSR imaging performance of 3 \times upscaling using only the actin cytoskeleton structure.

DFCAN model. The architecture of DFCAN is illustrated in Extended Data Fig. 3, which begins with a convolutional layer and a Gaussian error linear unit (GELU)³². GELU activation function is formulated as

$$\text{GELU}(x) = 0.5x \left(1 + \text{erf}\left(\frac{x}{\sqrt{2}}\right) \right) \quad (1)$$

where $\text{erf}(\cdot)$ is the error function, which can be formulated as

$$\text{erf}(x) = \frac{2}{\sqrt{\pi}} \int_0^x e^{-t^2} dt \quad (2)$$

The output of GELU is followed by four identical residual groups (RG), each of which consists of four Fourier channel attention blocks (FCAB) and a skip connection. The operation of a RG is denoted as

$$\text{RG}(x) = x + \text{FCAB}^{(4)}(x) \quad (3)$$

where

$$\text{FCAB}^{(n)}(x) = \underbrace{\text{FCAB}(\text{FCAB}(\dots \text{FCAB}(x)))}_{n \times \text{FCAB}} \quad (4)$$

x denotes the input feature maps of the RG. The structure of FCAB is illustrated in Extended Data Fig. 3. In each FCAB, feature maps are rescaled in a channelwise manner as follows:

$$\text{FCAB}(x) = x + y \times f(W_U \delta(W_D \varphi(y))) \quad (5)$$

where

$$y = \text{GELU}[\text{Conv}\{\text{GELU}[\text{Conv}\{x\}]\}] \quad (6)$$

$$\varphi(y) = \text{Pooling}_{\text{global}}(\text{ReLU}[\text{Conv}\{\text{abs}(\text{FFT}(y))^\gamma\}]) \quad (7)$$

$\text{FFT}(\cdot)$ represents the fast Fourier transform and γ is applied for enhancing the contributions of high-frequency components. $\text{Pooling}_{\text{global}}$ represents the global average pooling layer, so that every component of $\varphi(y)$ can be interpreted as a representative value of each feature map. W_D and W_U are the downscaling and upscaling weights, respectively, both of which are realized by 1×1 convolutional layers in the network. $f(\cdot)$ and $\delta(\cdot)$ are the sigmoid activation function and rectified linear unit (ReLU) activation function, respectively. Together, they result in a gating mechanism that can self-adaptively calculate the final rescaling factors.

The output of the last RG is fed into a convolutional layer activated by a GELU activation function. Then a pixel shuffle layer, a convolutional layer and a sigmoid activation layer are used to upscale the image to the same size as the GT image to accommodate the inferred high-frequency information. Finally, the network outputs a monochrome grayscale SR image.

The objective function, also called the loss function, of DFCAN is defined as a combination of MSE loss and SSIM loss. MSE loss ensures pixelwise accuracy and equalizes the dynamic range of prediction, and SSIM loss enhances the structural similarity of the output. If we define \hat{Y} as the output of DFCAN, Y as the corresponding GT and (w, h) as the pixel size of output image, then the objective function can be formulated as

$$L_{\text{DFCAN}}(\hat{Y}, Y) = \frac{1}{w \times h} \sum_{i=1}^{w \times h} (\hat{Y}_i - Y_i)^2 + \lambda \times [1 - \text{SSIM}(\hat{Y}, Y)] \quad (8)$$

where λ is a scalar weight used to balance the relative contributions of SSIM and MSE, which is set to 0.1 in most cases in the paper.

DFGAN model. The DFGAN is constructed based on the conditional generative adversarial network (cGAN)³³ framework, which consists of two models: one is the generative model G that learns the data distribution and performs the image transformation, the other is the discriminative model D that distinguishes if an image came from training data or was generated by the generator G . G takes low-resolution fluorescence images as input, and its output is an upscaled SR image. The discriminator D takes the output image from G or a GT SR image as input, and provides a score that reflects the probability of the input image being the GT. In the DFGAN framework, a deeper DFCAN acts as G (Supplementary Note 5), and D is constructed based on conventional CNN architecture (Extended Data Fig. 3). D consists of 12 convolutional layers, and the output of each convolutional layer is activated by a LeakyReLU activation function with a leaky factor of $\alpha = 0.1$, which can be formulated as

$$\text{LeakyReLU}(x, \alpha) = \max(0, x) - \alpha \max(0, -x) \quad (9)$$

Then the output of the last LeakyReLU activation function is fed into a global pooling layer and two fully connected layers followed by a sigmoid activation function. After that, D outputs the estimated probability.

The objective function of G and D , hereafter denoted as $L_{G|D}$ and L_D , respectively, are defined separately. The G objective function $L_{G|D}$ is the sum of two terms: SR error, which penalizes the difference between the G output and GT image, and discriminative error, which is related to the probability calculated by D . $L_{G|D}$ can be formulated as

$$L_{G|D}(X, Y) = L_{SR}(X, Y) + L_D(X) \\ = \beta \left(\frac{1}{w \times h} \sum_{i=1}^{w \times h} (G(X)_i - Y_i)^2 + \lambda \times [1 - SSIM(G(X), Y)] - \gamma \log(D(G(X))) \right) \quad (10)$$

where X is the input low-resolution image and Y is the SR target image. β , γ and λ are scalar weighting factors to balance the corresponding terms, which are set empirically to $\beta=0.1$, $\gamma=1$, $\lambda=0.1$ for best performance in our experiments, although the final results are not very sensitive to these parameters. The D objective function is defined as the binary cross-entropy. Taking \hat{y} as the output of D and y as the GT, then L_D can be described as

$$L_D(\hat{y}, y) = -y \log(\hat{y}) - (1 - y) \log(1 - \hat{y}) \quad (11)$$

The training process of G and D is just like a two-player game. From $L_{G|D}$ and L_D we can see that the objective of G is to fool D taking its output as ground truth, and in contrary, the objective of D is to determine if the input image is from G or ground truth. The G and D are trained in an interleaved scheme, so they compete against each other and finally reach an equilibrium state.

Fourier channel attention versus spatial channel attention. To compare the performance of the FCA mechanism (Extended Data Fig. 4a) with the SCA (Extended Data Fig. 4b), which was implemented in the squeeze-and-excitation (SE) block¹⁵ and RCAN⁵, we replaced the FCA in DFCAN with the SCA, resulting in a deep spatial channel attention network (DSCAN). Moreover, by removing the FCA in DFCAN, we constructed a modified ResNet for comparison. We trained the DLSR models of DFCAN, DSCAN and ResNet with simulated data of tubular structure (Supplementary Note 8) consisting of 10,000 pairs of WF (128×128 pixels) and GT-SIM (256×256 pixels) images with average photon count ranging from 5 to 100. Each model is evaluated with 1,000 validation image pairs for every 2,000 training iterations. As shown in Extended Data Fig. 4e, DFCAN achieves faster convergence and lower validation NRMSE than the other two networks. To further test if the FCA mechanism can be applied generally onto other types of neural network architectures, we implemented FCA in two widely used networks: U-net¹⁸ and DenseNet¹⁹. The U-net was constructed with three downsampling blocks and three upsampling blocks, and we put the FCA or SCA module at the beginning of each downsampling block, and at the end of each upsampling block, respectively (Extended Data Fig. 4c). The resulting networks were named U-net-FCA and U-net-SCA, respectively. The DenseNet consisted of three dense blocks interleaved with two transition layers. Each dense block was composed of eight densely connected ReLU-Conv modules, and each transition layer was composed of a ReLU activation and 1×1 convolutional layer. We implemented FCA and SCA modules at the end of each dense block to produce DenseNet-FCA and DenseNet-SCA networks, respectively (Extended Data Fig. 4d). All of these U-net or DenseNet based models were trained with simulated data of tubular structure. Extended Data Fig. 4f,g,h shows that FCA-based models infer the fine structures of crisscrossing tubular structures more precisely than the corresponding models based on SCA.

Image preprocessing and training. For each type of specimen and each imaging modality, we acquired a total of ~50 groups of WF (512×512 pixels) and GT-SIM (1,024×1,024 pixels) or GT-NLSIM (1,536×1,536 pixels) images. Each group contained nine escalating fluorescence levels. To generate the training dataset, we selected ~35 groups of original data (Supplementary Table 5), and applied random cropping, horizontal/vertical flipping and rotation transformation to further enrich the training dataset, which eventually generated ~20,000 pairs of WF (128×128 pixels) and GT-SIM (256×256 pixels) images, that is, ~2,200 pairs for each fluorescence level. For each type of DLSR network, a dedicated model was trained with the data of all fluorescence levels belonging to the same type of specimen. To generate the testing dataset, the remaining ~15 groups of data were augmented to a dataset of WF (256×256 pixels) and GT-SIM (512×512 pixels), and these paired images were then classified into 16 fluorescence levels ranging from 25 to 600 according to the average photon count (that is, the expressing level of specific cell). Each fluorescence level was ensured to possess more than 100 images.

The training and inference were performed on a computer workstation equipped with a Xeon(R) Gold 6134 CPU at 3.20 GHz (Intel) and two RTX 2080Ti graphic processing cards (NVIDIA) with python v.3.6, Tensorflow v.1.11.0 and Keras v.2.2.4. During the training process, we used the Adam optimizer and a batch size of two to six according to network scale. Taking the training process of CCPs as example, for the non-GAN methods of SRCNN, EDSR and DFCAN, we initialized the networks randomly and trained the models with a typical starting learning rate of 1×10^{-4} . The final models of SRCNN, EDSR, DFCAN and RCAN were trained for about 70,000, 150,000, 200,000 and 500,000 minibatch iterations, which took about 10, 120, 24 and 120h. For the GAN-based methods of Pix2Pix,

CMGAN and DFGAN, we also randomly initialized the networks, and trained the generative models and discriminative models with typical starting learning rates of 2×10^{-5} and 1×10^{-4} , respectively. The final models of Pix2Pix, CMGAN and DFGAN were trained for about 50,000, 90,000 and 80,000 minibatch iterations, which took about 20, 120 and 80h. In each iteration, G and D were updated three times and twice, respectively. The representative plots of validation NRMSE during the training processes of different networks are shown in Supplementary Fig. 13. The training time could be reduced by transfer learning and mix-precision training. Once the networks were trained, all of these DLSR models typically took less than 1 s to reconstruct an SR image of 1,024×1,024 pixels.

Image normalization and assessment metrics calculation. In this work, we examined the three metrics of NRMSE, MS-SSIM and resolution to assess the overall performance of a given DLSR model across the ranges of fluorescence intensity, structure complexity and upscaling factor, to finally generate the assessment matrix. Image normalization and assessment metrics calculation were performed on a MATLAB 2017b. NRMSE measures pixelwise grayscale error with respect to GT, so the NRMSE score of a DLSR image is inversely correlated to its quantifiability.

Because the DLSR images inferred from WF images of distinct fluorescence intensity and the corresponding GT image usually differ in the dynamic range, we normalize them to a common range following a commonly used procedure¹⁰. In detail, we first perform percentile-normalization for every GT image Y :

$$\text{Norm}_p(Y, p_{\text{low}}, p_{\text{high}}) = \frac{Y - \text{percentile}(Y, p_{\text{low}})}{\text{percentile}(Y, p_{\text{high}}) - \text{percentile}(Y, p_{\text{low}})} \quad (12)$$

where percentile (X, p) outputs the intensity value ranks $p\%$. p_{low} and p_{high} are 0.1 and 99.9 typically in this work. Next, we perform image registration for each DLSR image \hat{Y} according to the cross-correlation (CC) between $\text{Norm}_p(Y, p_{\text{low}}, p_{\text{high}})$ and \hat{Y} . The cross-correlation can be calculated by

$$\text{CC}(\hat{Y}, \text{Norm}_p(Y, p_{\text{low}}, p_{\text{high}})) = \text{IFFT}\left(\overline{\text{FFT}(\text{Norm}_p(Y, p_{\text{low}}, p_{\text{high}}))} \cdot \text{FFT}(\hat{Y})\right) \quad (13)$$

where FFT(\cdot) denotes fast Fourier transform, IFFT(\cdot) denotes inverse fast Fourier transform and $\overline{\text{FFT}(Y)}$ is the conjugate of $\text{FFT}(Y)$. Then a linear transformation is applied to each DLSR image after registration \hat{Y}_{regis} :

$$\text{Trans}_{\text{linear}}(\hat{Y}_{\text{regis}}) = \alpha \hat{Y}_{\text{regis}} + \beta \quad (14)$$

where α and β are chosen by solving the convex optimization problem

$$\arg \min_{\alpha, \beta} \|\alpha \hat{Y}_{\text{regis}} + \beta - \text{Norm}_p(Y, p_{\text{low}}, p_{\text{high}})\|_2 \quad (15)$$

where $\|\cdot\|_2$ denotes L2-norm. Apparently, the optimized α and β leads to an MSE-minimized linear transformation of \hat{Y}_{regis} , and thus it scales and translates every pixel of the DLSR image to match the dynamic range of GT.

The normalization or linear transformation is applied to all images used to calculate the three metrics. NRMSR and MS-SSIM are defined as

$$\text{NRMSE}(\hat{Y}, Y) = \sqrt{\frac{1}{w \times h} \sum_{i=1}^{w \times h} (\hat{Y}_i - Y_i)^2 / (\max(Y) - \min(Y))} \quad (16)$$

$$\text{MS-SSIM}(\hat{Y}, Y) = [l_M(\hat{Y}, Y)]^{\alpha_M} \cdot \prod_{j=1}^M [c_j(\hat{Y}, Y)]^{\beta_j} [s_j(\hat{Y}, Y)]^{\gamma_j} \quad (17)$$

where the $l_j(\hat{Y}, Y)$, $c_j(\hat{Y}, Y)$ and $s_j(\hat{Y}, Y)$ are the measures of luminance, contrast and structure corresponding to scale j , and the exponents α_M , β_j and γ_j are used to adjust the relative weighting of different components; they are typically set as $\alpha_j=\beta_j=\gamma_j$ for $\sum_{j=1}^M \gamma_j = 1$ (Supplementary Note 2).

Resolution evaluation is performed by decorrelation analysis³⁴. This method does not estimate the theoretical resolution stated by Abbe, but rather the highest frequency from the local maxima of the decorrelation functions, which is a comprehensive measurement of resolution and SNR (Supplementary Note 3 and Supplementary Fig. 14). The decorrelation function is defined as

$$d(r) = \frac{\int \text{Re}\{I(k)I_n(k)M(k, r)\} dk_x dk_y}{\sqrt{\int |I(k)|^2 dk_x dk_y \int |I_n(k)M(k, r)|^2 dk_x dk_y}} \quad (18)$$

where $k=[k_x, k_y]$ denotes Fourier space coordinates, $I(k)$ represents the Fourier transform of the test image, $I_n(k)=I(k)/|I(k)|$ is the normalization for the Fourier spectrum, and $M(k, r)$ is a binary circular mask of radius $r \in [0, 1]$.

Calculation of average photon count. In this work, we used the metric of average photon count to quantitatively measure the signal level of the raw SIM images. The

average photon count of a given image X was calculated by the following steps: (1) subtracting the average background of the camera, which is ~ 100 in our case; (2) using a Gaussian low-pass filter of standard deviation five pixels to blur the original image X , and then perform the aforementioned percentile-normalization on the filtered image; (3) extracting the feature-only regions of the normalized image with a threshold of 0.2; (4) calculating the average sCMOS count of the thresholded image; (5) converting the average sCMOS count into average photon count by a conversion factor of 0.6026 photons per count, which was measured by following the protocol provided by the manufacturer (Hamamatsu).

Structural complexity. The structural complexity measures the density and intricacy of a specific biological specimen. For a given biological SIM image I , consisting of $M \times N$ pixels, we define its structural complexity as its grayscale mean gradient (MG):

$$\text{MG}(I) = \frac{1}{M \times N} \sum_{i=1}^M \sum_{j=1}^N \sqrt{\frac{\left(\frac{\Delta I}{\Delta x}\right)_{ij}^2 + \left(\frac{\Delta I}{\Delta y}\right)_{ij}^2}{2}} \quad (19)$$

Typical gradient maps and corresponding MGs of CCPs, ER, MTs and F-actin are shown in Supplementary Fig. 1a–c. For each type of biological specimen, we employed its mean MG (averaged from the MG scores of all its GT-SIM images in the BioSR dataset) to represent its structural complexity. As shown in Supplementary Fig. 1, the structural complexity increases from punctate CCPs, reticular ER and string-like MTs to intricate F-actin.

Imaging conditions of live-cell experiments. To reconstruct the DFCAN- or DFGAN-SISR images shown in Fig. 4, we acquired the raw images in WF mode for 1,230 frames at 2-s intervals (Fig. 4a) and 931 frames at 2-s intervals (Fig. 4e). The WF raw image of Fig. 4a,c,d were acquired with 488 nm illumination intensity of 7 W cm^{-2} , 24 ms exposure time for PHB2-mEmerald, and 560 nm illumination intensity of 34 W cm^{-2} , 24 ms exposure time for TFAM-mCherry; Fig. 5e were acquired with 488 nm illumination intensity of 3 W cm^{-2} , 12 ms exposure time for PHB2-mEmerald, and 560 nm illumination intensity of 8 W cm^{-2} and 12 ms exposure time for TFAM-mCherry. To reconstruct the DFCAN- or DFGAN-SIM images shown in Fig. 6, we acquired the raw images in SIM mode of three-phase \times three-orientation for 402 frames at 5-s intervals (Fig. 6a), 421 frames at 2-s intervals (Fig. 6c) and 311 frames at 2-s intervals (Fig. 6d). Each raw image of Fig. 6a,b was acquired with a 488 nm illumination intensity of 15 W cm^{-2} and 10 ms exposure time for Lifeact-mEmerald, and 560 nm illumination intensity of 140 W cm^{-2} and 10 ms exposure time for clathrin-mCherry. Each raw image in Fig. 6c was acquired with 488 nm illumination intensity of 35 W cm^{-2} and 2 ms exposure time for PHB2-mEmerald, and 560 nm illumination intensity of 150 W cm^{-2} and 5 ms exposure time for KDEL-mCherry. Each raw image of Fig. 6d,e was acquired with 488 nm illumination intensity of 35 W cm^{-2} and 2 ms exposure time for PHB2-mEmerald, and 560 nm illumination intensity of 60 W cm^{-2} and 5 ms exposure time for KDEL-mCherry.

Cell culture. The COS-7 cell line was grown in Dulbecco's Modified Eagle Medium (DMEM) (GIBCO) supplemented with 10% fetal bovine serum (GIBCO) and 1% penicillin/streptomycin at 37°C and 5% CO_2 until 60–80% confluence was reached. After coating 25-mm coverslips with 50 mg ml^{-1} collagen for 1 h, cells were seeded onto the coverslips to achieve $\sim 70\%$ confluence before transfection. The manufacturer's protocol for Lipofectamine 3000 (Invitrogen) was employed for transient transfections. The plasmid constructs used in this study include Lifeact-mEmerald, clathrin-mEmerald, enconsin-mEmerald, Lifeact-SkylineNS, clathrin-mCherry, PHB2-mEmerald, TFAM-mCherry and KDEL-mCherry.

Statistics and reproducibility. Each DLSR model was trained independently three times with the same training data and hyperparameters, then the model with the lowest validation NRMSE was adopted for further assessment. Experiments in Figs. 1a,b, 3a, 5a–d and Extended Data Fig. 2 were repeated with 120 test images for each type of specimens and upscaling factors, all achieving similar results. All data in the assessment matrices or curves were averaged from tests of more than 100 images. Figures 2d and 5f were plotted in Tukey box-and-whisker format. The box extends from the 25th and 75th percentiles and the line in the middle of the

box indicates the median. The upper whisker represents the larger value between the largest data point and the 75th percentiles plus $1.5 \times$ the interquartile range (IQR), and the lower whisker represents the smaller value between the smallest data point and the 25th percentiles minus $1.5 \times$ the IQR. Data points larger than the upper whisker or smaller than the lower whisker are identified as outliers, which are displayed as black crosses.

Reporting Summary. Further information on research design is available in the Nature Research Reporting Summary linked to this article.

Data availability

The BioSR dataset including more than 2,200 pairs of LR–SR images covering four biology structures, nine SNR levels and two upscaling factors are publicly accessible at figshare repository (<https://doi.org/10.6084/m9.figshare.13264793>). Source data are provided with this paper.

Code availability

The tensorflow codes of DFCAN and DFGAN, several representative trained models, as well as some example images for testing are publicly available at <https://github.com/qcl7-THU/DL-SR>.

References

32. Hendrycks, D. & Gimpel, K. Gaussian error linear units (GELUs). Preprint at <https://arxiv.org/abs/1606.08415> (2016).
33. Goodfellow, I. et al. Generative adversarial nets. In *Proc. Advances in Neural Information Processing Systems 27 (NIPS)* (eds. Ghahramani, Z. et al.) 2672–2680 (MIT Press, 2014).
34. Descloux, A., Grussmayer, K. S. & Radenovic, A. Parameter-free image resolution estimation based on decorrelation analysis. *Nat. Methods* **16**, 918–924 (2019).

Acknowledgements

This work was supported by grants from the National Natural Science Foundation of China (NSFC; nos. 91754202, 31827802, 31800717, and 62088102); Ministry of Science and Technology (MOST; nos. 2017YFA0505301 and 2016YFA0500203); Chinese Academy of Sciences (CAS; nos. XDB19040101 and ZDBS-LY-SM004); The Youth Innovation Promotion Association of Chinese Academy of Sciences (no. 2020094); China Postdoctoral Science Foundation (no. BX20190355); and the Tencent Foundation through the XPLORER PRIZE.

Author contributions

Dong Li conceived the project. Dong Li and Q.D. supervised the research. Dong Li, C.Q. and Di Li designed the experiments. Di Li, Y.G., C.L. and T.J. prepared samples and performed experiments. C.Q., Di Li, Y.G. and C.L. analyzed the data with conceptual advice from Dong Li. C.Q. and Di Li composed the figures and videos under the supervision of Dong Li. Dong Li, C.Q. and Q.D. wrote the manuscript with input from all authors. All authors discussed the results and commented on the manuscript.

Competing interests

Dong Li, C.Q., Di Li and Q.D. have a pending patent application on the presented framework.

Additional information

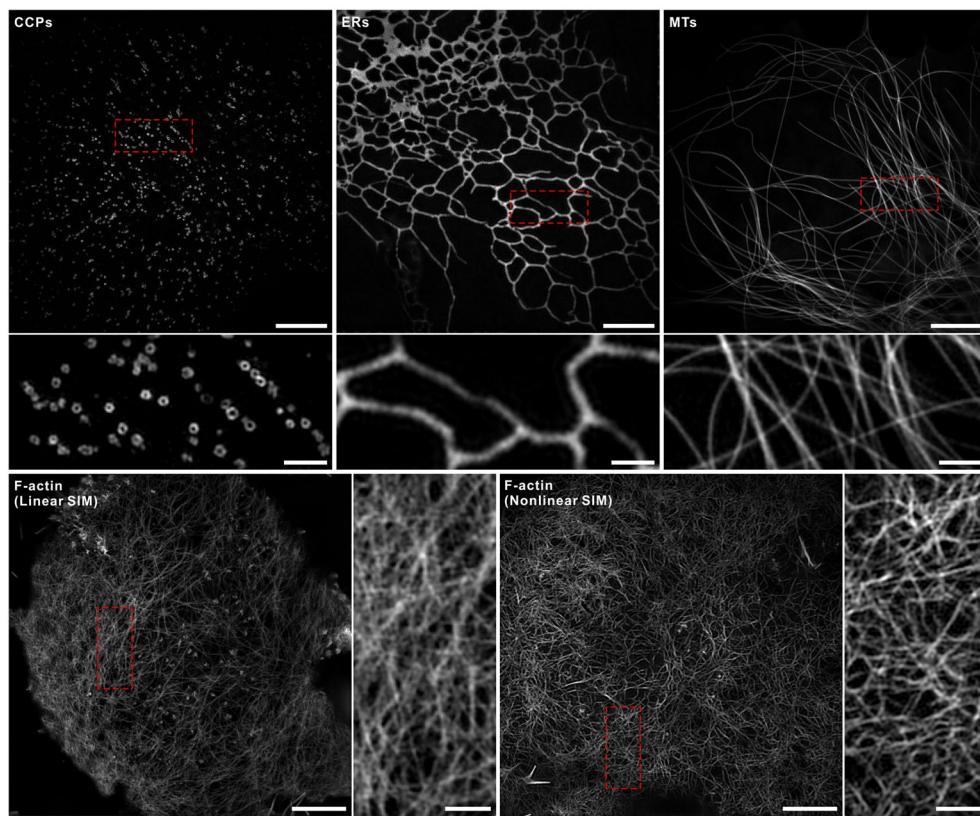
Extended data is available for this paper at <https://doi.org/10.1038/s41592-020-01048-5>.

Supplementary information is available for this paper at <https://doi.org/10.1038/s41592-020-01048-5>.

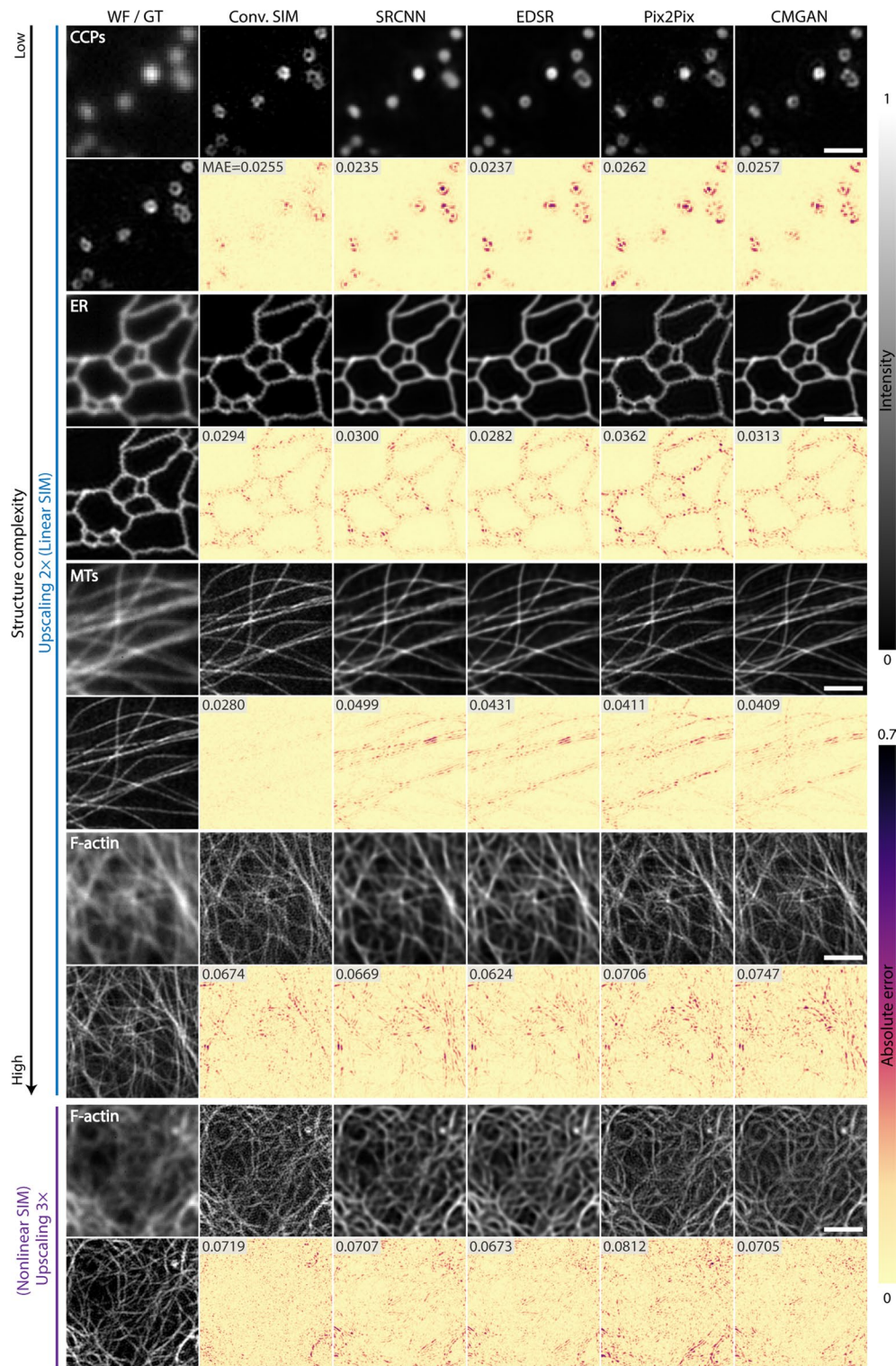
Correspondence and requests for materials should be addressed to Q.D. or D.L.

Peer review information Rita Strack was the primary editor on this article and managed its editorial process and peer review in collaboration with the rest of the editorial team.

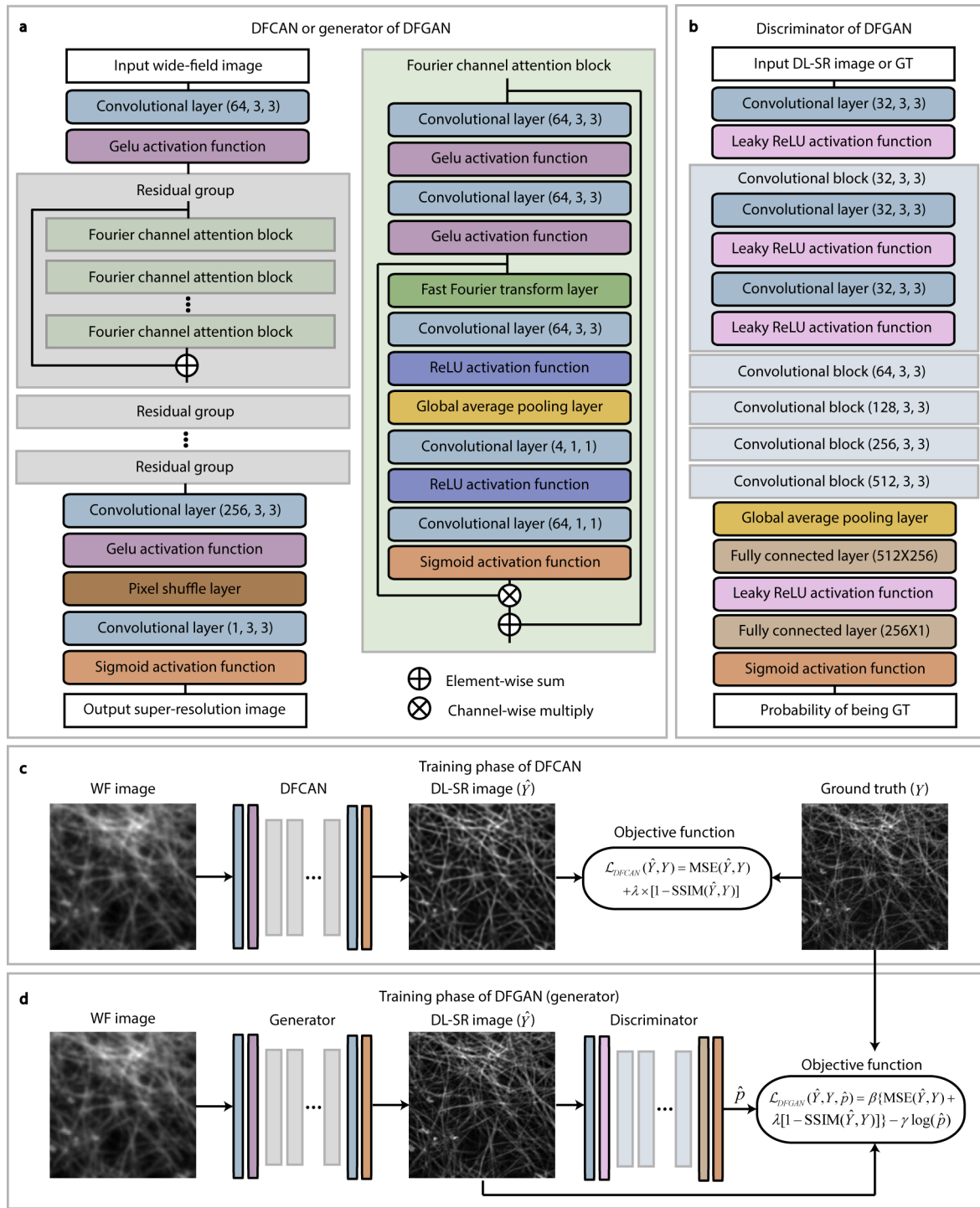
Reprints and permissions information is available at www.nature.com/reprints.



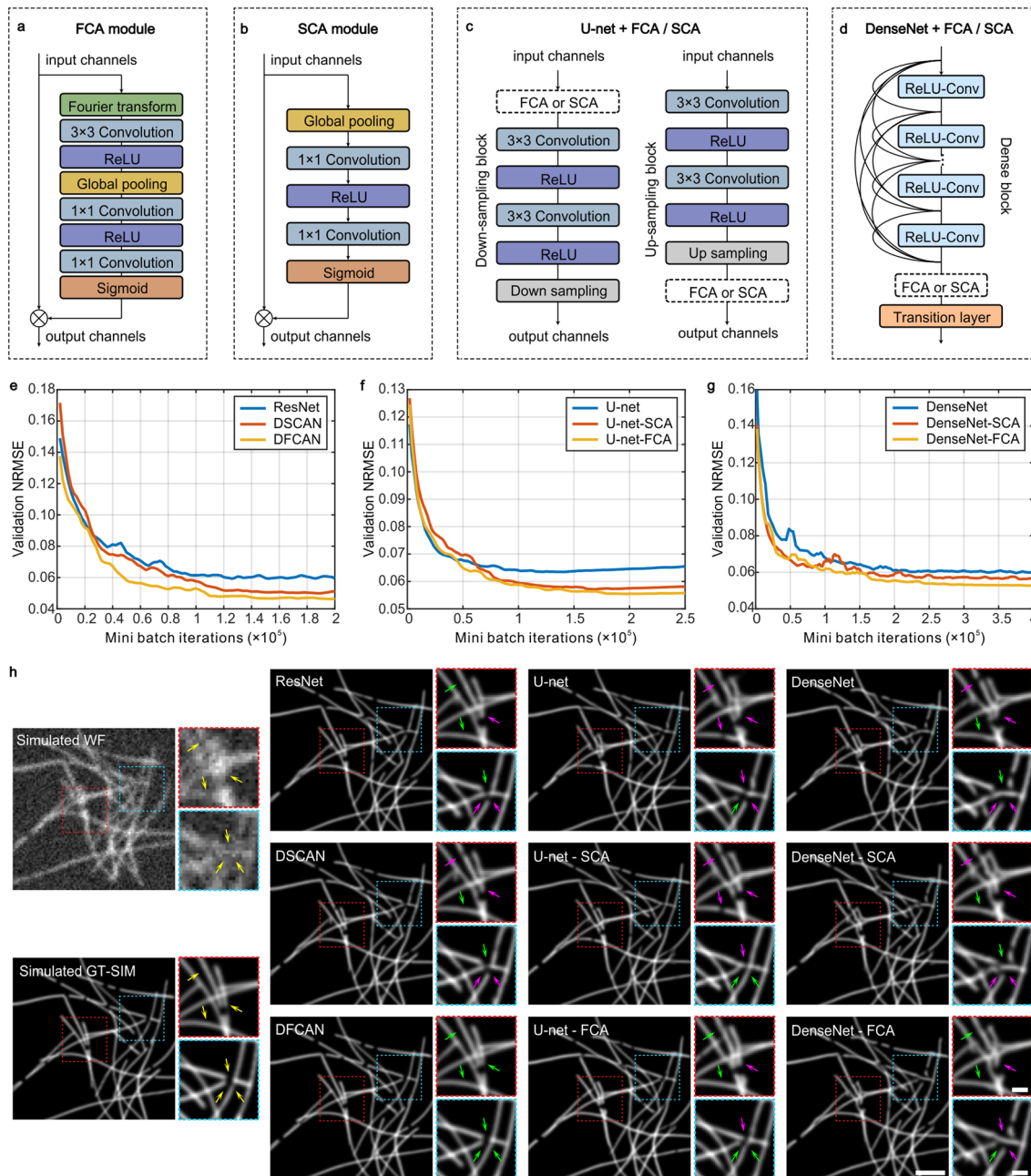
Extended Data Fig. 1 | Representative GT-SIM images of CCPs, ER, MTs, F-actin (linear SIM) and F-actin (nonlinear SIM). Scale bar: 5 μm , and 1 μm (zoom-in regions). Gamma values: 0.8 for F-actin images of both linear and nonlinear SIM. For each type of specimens, experiments were repeated independently for more than 100 test images with similar characteristics and performance.



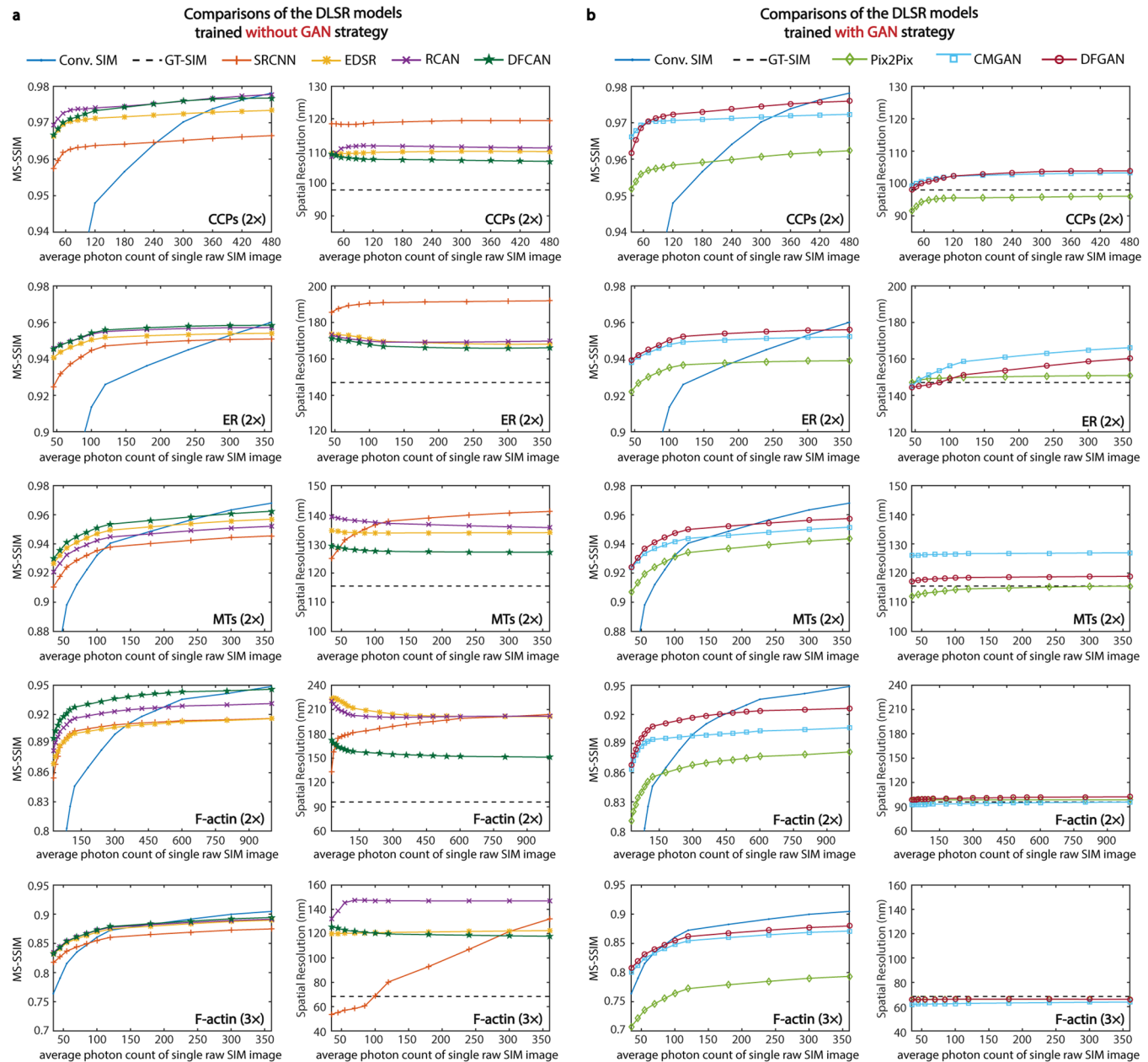
Extended Data Fig. 2 | Representative super-resolution images inferred from the wide-field diffraction-limited images of medium fluorescence intensity by the four DSLR models. The difference images with respect to ground truth (GT) are below the corresponding DSLR images. The mean absolute error (MAE) of each difference image is labeled in its top left corner. Scale bar: 0.75 μm for CCPs; 1.5 μm for other specimens. Gamma values: 0.6 for the F-actin images of upscaling 3 \times .



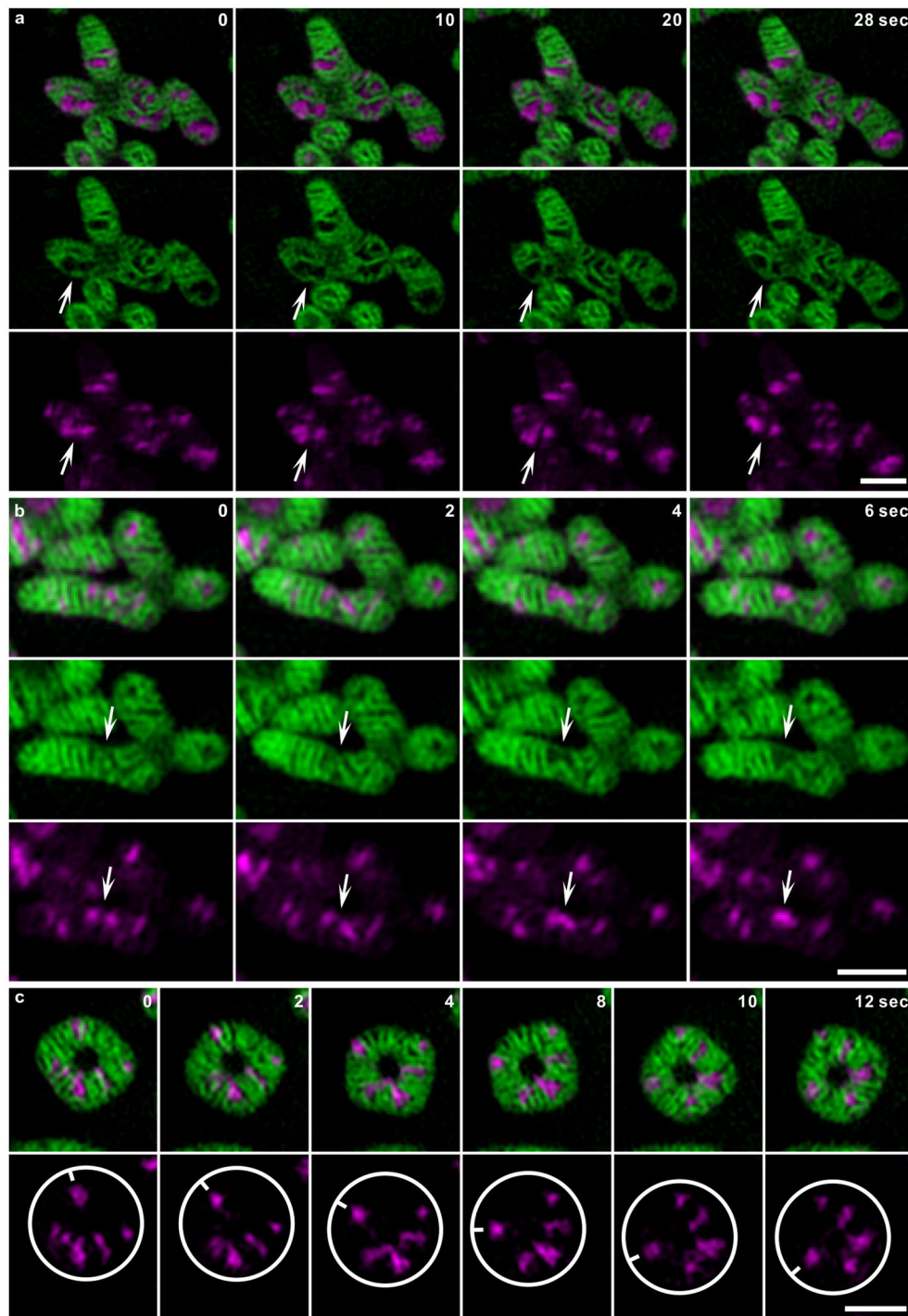
Extended Data Fig. 3 | Network architecture of DFCAN and DFGAN. **a**, The architecture of DFCAN or the generator of DFGAN. **b**, The architecture of the discriminator of DFGAN. **c**, Schematic of the training process of DFCAN. **d**, Schematic of the training process of the generator of DFGAN. The generator and the discriminator were trained alternatively. The discriminator's parameters remained unchanged during each training step of the generator.



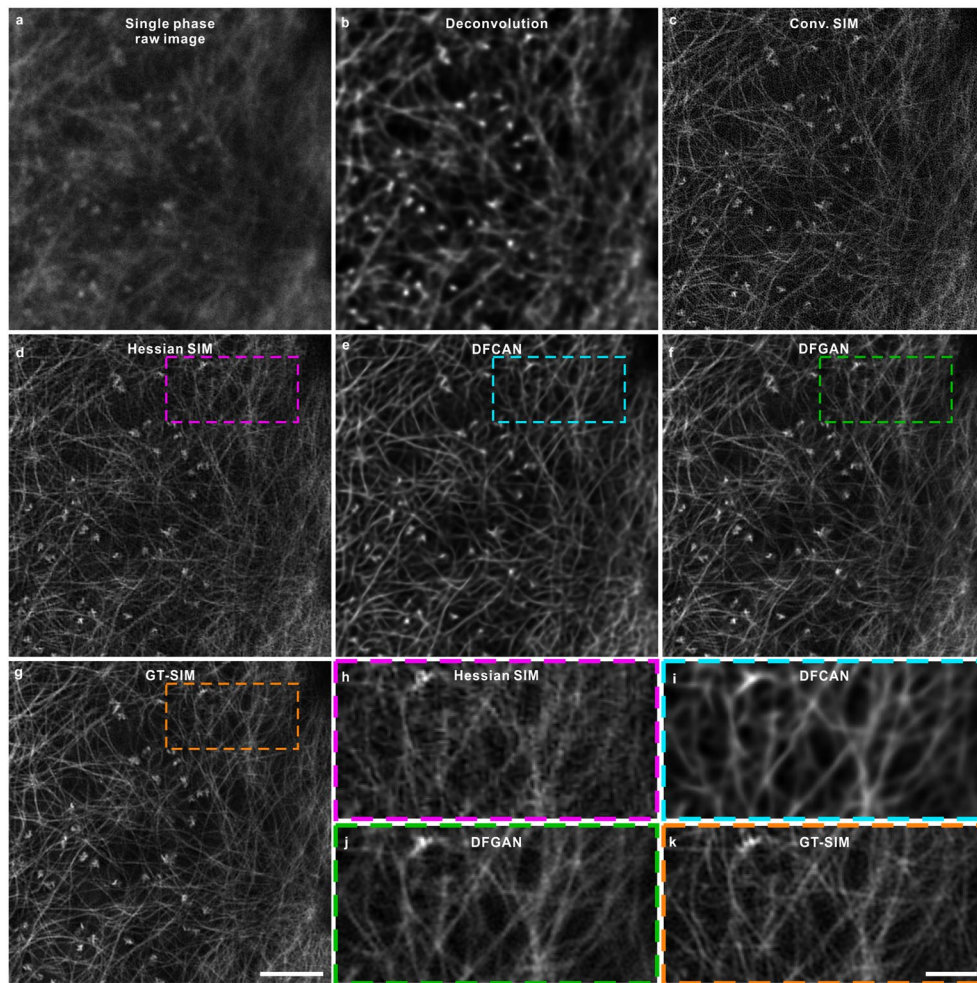
Extended Data Fig. 4 | Comparison of Fourier channel attention (FCA) and spatial channel attention (SCA) mechanism. **a, b,** The architecture of FCA (a) and SCA (b). **c, d,** The schematic illustrating the positions where the FCA or SCA module was added into U-net (c) and DenseNet (d). **e, f, g,** Comparisons of the validation NRMSE achieved over the training process of (e) DFCAN, a modified ResNet from DFCAN without using FCA-modules, and deep spatial channel attention network (DSCAN), whose architecture is the same as DFCAN except for replacing the FCA- with SCA modules. (f) conventional U-net, U-net with SCA (named U-net-SCA), and U-net with FCA (named U-net-FCA); (g) conventional DenseNet, DenseNet with SCA (named DenseNet-SCA), and DenseNet with FCA (named DenseNet-FCA). **h,** Representative SISR images of simulated tubular structure inferred by the aforementioned DLSR models. In each magnified image, the green arrows indicate the features correctly inferred, whereas magenta arrows indicate the features wrongly inferred by specific DLSR model. Yellow arrows indicate the same features in the corresponding GT-SIM and wide-field images for reference. Scale bar: 1 μ m, and 0.3 μ m for both magnified regions. Experiments were repeated independently for 30 test images, achieving similar results.



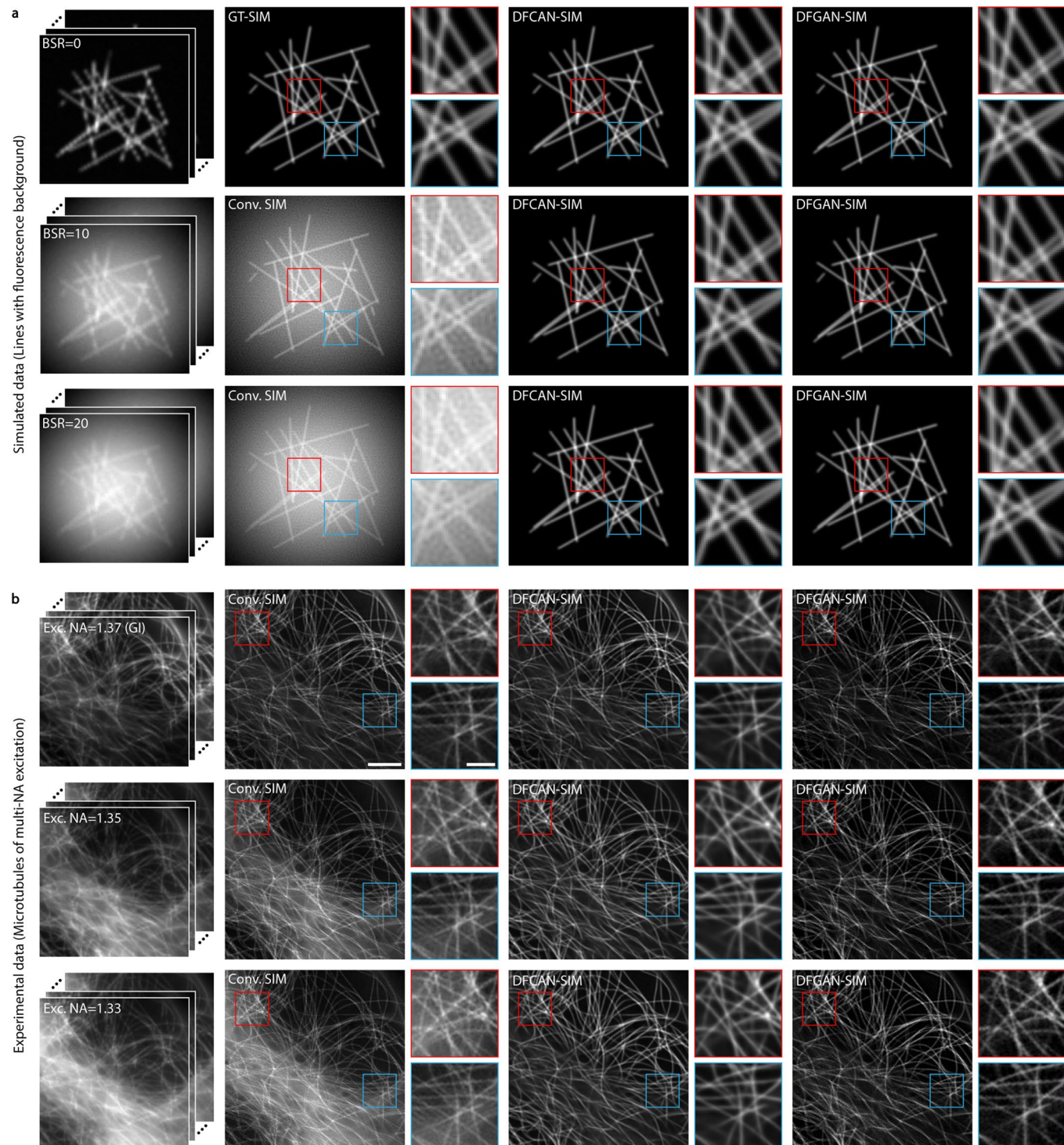
Extended Data Fig. 5 | MS-SSIM and resolution comparisons of SISR images generated by different DLSR models. MS-SSIM and resolution comparisons of the seven DLSR models that are classified into two categories: non-GAN models (a) and GAN-based models (b) in the cases of CCPs, ER, MTs, and F-actin (upscale 2x), and F-actin (upscale 3x).



Extended Data Fig. 6 | Live-cell GI-SIM images confirming the phenomena observed in Fig. 4. **a**, Time-lapse GI-SIM images of a nucleoid fission event concomitant with the formation of a new cristae in between. **b**, Time-lapse GI-SIM images of a nucleoids fusion event concomitant with the recession of the intermediate cristae. **c**, Time-lapse GI-SIM images illustrating the bidirectional rotation of circular mitochondrial tubes. Lower row shows that nucleoids inside mitochondria change their orientation accordingly. Scale bar: 1 μm (a-c). Experiments were repeated independently for $n=10$ COS-7 cells, all showing similar characteristics and performance.

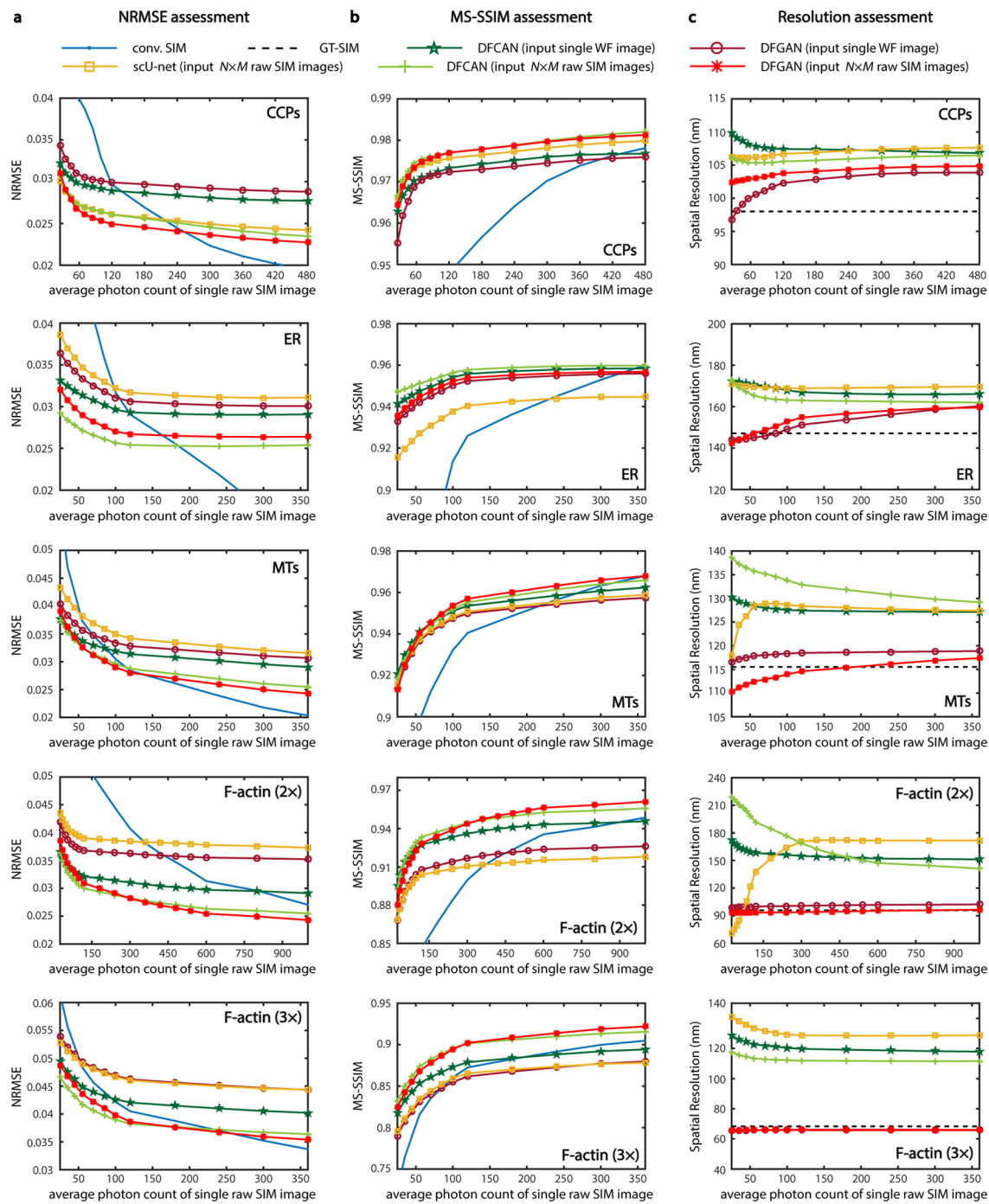


Extended Data Fig. 7 | SR imaging comparisons of conventional non-deep-learning methods and DFCAN or DFGAN. **a**, Single phase raw SIM image acquired at relatively low-fluorescence (average photon count = 120). **b**, Deconvolved image with Richardson-Lucy algorithm (NRMSE = 0.0755, MS-SSIM = 0.7512, Resolution = 243 nm). **c**, Conventional SIM image (NRMSE = 0.0781, MS-SSIM = 0.7832, Resolution = 96 nm). **d**, Hessian algorithm²⁷ denoised image ($\mu=150$, $\sigma=0$) after Conventional SIM reconstruction (NRMSE = 0.0622, MS-SSIM = 0.8584, Resolution = 101 nm). **e**, **f**, SIM image reconstructed by **(e)** DFCAN (NRMSE = 0.0593, MS-SSIM = 0.8665, Resolution = 139 nm) and **(f)** DFGAN (NRMSE = 0.0586, MS-SSIM = 0.8680, Resolution = 97 nm). **g**, GT-SIM image acquired at high SNR. **h-k**, magnified images of **(h)** Hessian-SIM, **(i)** DFCAN, **(j)** DFGAN, and **(k)** GT-SIM from the boxed regions in corresponding images. Scale bar: 3 μ m; 1 μ m in magnified image. Experiments were repeated with more than 100 test images, achieving similar results.

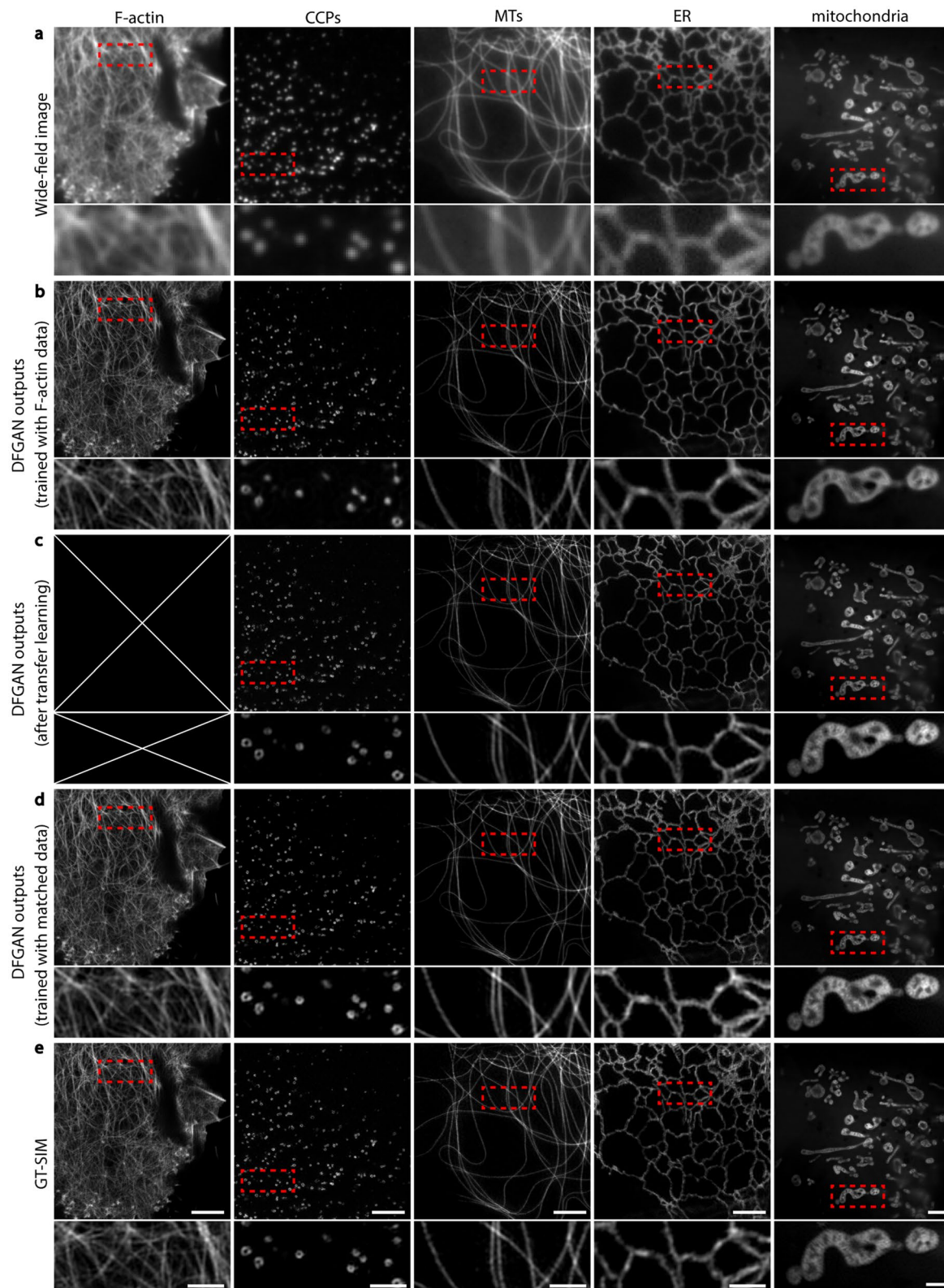


Extended Data Fig. 8 | The robustness of DFCAN and DFGAN algorithms to reconstruct the raw SIM images of high out-of-focus background.

a, DFCAN and DFGAN can reconstruct the simulated raw images of background-to-signal ratio as high as 20, although the Moiré fringes in the raw images are so obscure that many reconstruction artifacts are riddled in the conventional SIM image. **b**, DFCAN and DFGAN also largely prevent the SR images from reconstruction artifacts, although the raw images are contaminated by large out-of-focus background because the used excitation NA (Exc. NA) is significantly lower than the critical NA for TIRF or grazing incidence (GI). Experiments in (a) and (b) were repeated with 20 images, achieving similar results.



Extended Data Fig. 9 | NRMSE, MS-SSIM and resolution comparisons of SIM image reconstruction by different DLSR models. NRMSE (a), MS-SSIM (b), and resolution (c) comparisons of DLSR images generated by scU-net input of $N \times M$ raw SIM images (yellow), DFCAN input of single WF image (dark green), DFCAN input of $N \times M$ raw SIM images (light green), DFGAN input of single WF image (dark red), DFGAN input of $N \times M$ raw SIM images (red) in the cases of CCPs (first row), ER (second row), MTs (third row), and F-actin (linear SIM, 2 \times upscaling) (fourth row), and F-actin (nonlinear SIM, 3 \times upscaling) (fifth row).



Extended Data Fig. 10 | Assessment of transfer learning capability of DFGAN. **a**, Representative raw SIM images of F-actin, CCPs, MTs, endoplasmic reticulum (ER), and mitochondria. **b**, The super-resolution images inferred by the same DFGAN network, which is trained with only F-actin images. **c**, SIM images reconstructed by the DFGAN networks after transfer learning for each type of specimen, which are initialized by the DFGAN network trained with only F-actin data (Supplementary Note 7). **d**, SIM images reconstructed by the DFGAN networks trained with corresponding datasets. **e**, The ground truth SIM images shown for reference. Scale bar: 3 μ m; 1 μ m for the zoom-in regions. Experiments were repeated with more than 50 test images for each type of specimens, achieving similar results.

Reporting Summary

Nature Research wishes to improve the reproducibility of the work that we publish. This form provides structure for consistency and transparency in reporting. For further information on Nature Research policies, see our [Editorial Policies](#) and the [Editorial Policy Checklist](#).

Statistics

For all statistical analyses, confirm that the following items are present in the figure legend, table legend, main text, or Methods section.

n/a Confirmed

- The exact sample size (n) for each experimental group/condition, given as a discrete number and unit of measurement
- A statement on whether measurements were taken from distinct samples or whether the same sample was measured repeatedly
- The statistical test(s) used AND whether they are one- or two-sided
Only common tests should be described solely by name; describe more complex techniques in the Methods section.
- A description of all covariates tested
- A description of any assumptions or corrections, such as tests of normality and adjustment for multiple comparisons
- A full description of the statistical parameters including central tendency (e.g. means) or other basic estimates (e.g. regression coefficient) AND variation (e.g. standard deviation) or associated estimates of uncertainty (e.g. confidence intervals)
- For null hypothesis testing, the test statistic (e.g. F , t , r) with confidence intervals, effect sizes, degrees of freedom and P value noted
Give P values as exact values whenever suitable.
- For Bayesian analysis, information on the choice of priors and Markov chain Monte Carlo settings
- For hierarchical and complex designs, identification of the appropriate level for tests and full reporting of outcomes
- Estimates of effect sizes (e.g. Cohen's d , Pearson's r), indicating how they were calculated

Our web collection on [statistics for biologists](#) contains articles on many of the points above.

Software and code

Policy information about [availability of computer code](#)

Data collection	All data were collected using a home-written control software. The methods and conclusions reported in this work is not specific to the control program, but can be generalized to other deep learning super-resolution modalities.
Data analysis	The data augmentation, data normalization and calculation of assessment matrices were performed with Matlab 2017b. The deep learning models were trained, validated and tested using python3.6, Tensorflow1.11.0, and Keras 2.2.4 . We have uploaded the source code of the Tensorflow implementation of DFCAN and DFGAN into GitHub (https://github.com/qc17-THU/DL-SR), and added the download information into the code availability section.

For manuscripts utilizing custom algorithms or software that are central to the research but not yet described in published literature, software must be made available to editors and reviewers. We strongly encourage code deposition in a community repository (e.g. GitHub). See the Nature Research [guidelines for submitting code & software](#) for further information.

Data

Policy information about [availability of data](#)

All manuscripts must include a [data availability statement](#). This statement should provide the following information, where applicable:

- Accession codes, unique identifiers, or web links for publicly available datasets
- A list of figures that have associated raw data
- A description of any restrictions on data availability

The BioSR dataset including more than 2200 pairs of LR-SR images covering four biology structures, nine SNR levels, and two upscaling-factors are publicly accessible at figshare repository (DOI: 10.6084/m9.figshare.13264793).

Field-specific reporting

Please select the one below that is the best fit for your research. If you are not sure, read the appropriate sections before making your selection.

- Life sciences Behavioural & social sciences Ecological, evolutionary & environmental sciences

For a reference copy of the document with all sections, see nature.com/documents/nr-reporting-summary-flat.pdf

Life sciences study design

All studies must disclose on these points even when the disclosure is negative.

Sample size	Sample size was not predetermined based on statistical calculations. But for every experiment in this study, we performed at least 10 replications to ensure reproducibility.
Data exclusions	There is no data excluded after input into deep neural network for afterwards training and test.
Replication	Each data in the assessment matrices or curves was averaged from the test results of more than 100 test images. The live-cell experiments in Fig. 4 and 6 were repeated for n=10 Cos-7 cells, all showing similar characteristics and performance. And other detailed sample size information is described in the corresponding legends of figures and the "Statistics and reproducibility" section of Methods.
Randomization	No randomization was used for experimental data. No sample randomization was performed in this study.
Blinding	The assessment of DLSR models were performed blindly with the data that were not included in the training process.

Reporting for specific materials, systems and methods

We require information from authors about some types of materials, experimental systems and methods used in many studies. Here, indicate whether each material, system or method listed is relevant to your study. If you are not sure if a list item applies to your research, read the appropriate section before selecting a response.

Materials & experimental systems		Methods	
n/a	Involved in the study	n/a	Involved in the study
<input checked="" type="checkbox"/>	<input type="checkbox"/> Antibodies	<input checked="" type="checkbox"/>	<input type="checkbox"/> ChIP-seq
<input type="checkbox"/>	<input checked="" type="checkbox"/> Eukaryotic cell lines	<input checked="" type="checkbox"/>	<input type="checkbox"/> Flow cytometry
<input checked="" type="checkbox"/>	<input type="checkbox"/> Palaeontology and archaeology	<input checked="" type="checkbox"/>	<input type="checkbox"/> MRI-based neuroimaging
<input checked="" type="checkbox"/>	<input type="checkbox"/> Animals and other organisms		
<input checked="" type="checkbox"/>	<input type="checkbox"/> Human research participants		
<input checked="" type="checkbox"/>	<input type="checkbox"/> Clinical data		
<input checked="" type="checkbox"/>	<input type="checkbox"/> Dual use research of concern		

Eukaryotic cell lines

Policy information about [cell lines](#)

Cell line source(s)	Cercopithecus aethiops kindney COS-7 cell line ATCC CRL-1651
Authentication	The Cos-7 cell line is not specifically authenticated in my lab.
Mycoplasma contamination	The cell line used in this study is not contaminated by mycoplasma.
Commonly misidentified lines (See ICLAC register)	There is no misidentified cell line used in this study.